DETERMINATION OF FRACTURE AND FATIGUE BEHAVIOURS OF 4340 STEEL

A THESIS SUBMITTED TO
THE GRADUATE SCHOOL OF NATURAL AND APPLIED SCIENCES
OF
MIDDLE EAST TECHNICAL UNIVERSITY

BY
GÖKÇE ŞEN

IN PARTIAL FULFILLMENT OF THE REQUIREMENTS
FOR
THE DEGREE OF MASTER OF SCIENCE
IN
METALLURGICAL AND MATERIALS ENGINEERING

MAY 2015

Approval of the thesis:

DETERMINATION OF FRACTURE AND FATIGUE BEHAVIOURS OF 4340 STEEL

submitted by **GÖKÇE ŞEN** in partial fulfillment of the requirements for the degree of **Master of Science in Metallurgical and Materials Engineering Department, Middle East Technical University** by,

Prof. Dr. Gülbin Dural Ünver
Dean, Graduate School of **Natural and Applied Sciences** _____

Prof. Dr. C. Hakan Gür
Head of Department, **Metallurgical and Materials Eng.** _____

Prof. Dr. Rıza Gürbüz
Supervisor, **Metallurgical and Materials Eng. Dept., METU** _____

Prof. Dr. Bilgehan Ögel
Co-Supervisor, **Metallurgical and Materials Eng. Dept., METU** _____

Examining Committee Members:

Prof. Dr. Ali Kalkanlı
Metallurgical and Materials Eng. Dept., METU _____

Prof. Dr. Rıza Gürbüz
Metallurgical and Materials Eng. Dept., METU _____

Prof. Dr. Bilgehan Ögel
Metallurgical and Materials Eng. Dept., METU _____

Dr. Koray Yurtışık
Metallurgical and Materials Eng. Dept., METU _____

Assoc. Prof. Dr. Kazım Tur
Metallurgical and Materials Eng. Dept., Atılım University _____

Date: 05.05.2015

I hereby declare that all information in this document has been obtained and presented in accordance with academic rules and ethical conduct. I also declare that, as required by these rules and conduct, I have fully cited and referenced all material and results that are not original to this work.

Name, Last Name : Gökçe Şen

Signature :

ABSTRACT

DETERMINATION OF FRACTURE AND FATIGUE BEHAVIOURS OF 4340 STEEL

Şen, Gökçe
M.S., Department of Metallurgical and Materials Engineering
Supervisor: Prof. Dr. Rıza Gürbüz
Co-Supervisor: Prof. Dr. Bilgehan Ögel

May 2015, 98 Pages

In this study both the characteristic and mechanical properties of received modified AISI 4340 steel -generally used in aeronautical and defense applications- has been examined. Mode I Fracture toughness (K_{IC}) tests have been conducted with two different directional specimens of RL and LR. Fatigue crack growth behaviors of directional specimens are compared and discussed at three different positive stress ratios (R) which are 0.1, 0.3 and 0.5 under constant amplitude loading. Walker equation is used to perform fatigue life calculations and the evaluation of test results for tensile loading. On the next step, the modified steel specimens are subjected to fully reversed stress cycle (R= -1) and the Paris-Erdogan law has been applied to all achieved data. The difference in the production of modified AISI 4340 steel (M4340) steps are correlated with the results and compared with commercial AISI 4340 steel theoretical information.

The obtained measurements show that the M4340 steel has higher hardness and toughness compared to standard AISI 4340 steel.

Keywords: AISI 4340 steel, Fatigue, Mode I fatigue crack growth rate, Walker equation, Low-carbon steel.

ÖZ

4340 ÇELİĞİNİN KIRILMA VE YORULMA ÖZELLİKLERİNİN İNCELENMESİ

Şen, Gökçe
Yüksek Lisans, Metalurji ve Malzeme Mühendisliği Bölümü
Tez Yöneticisi: Prof. Dr. Rıza Gürbüz
Ortak Tez Yöneticisi: Prof. Dr. Bilgehan Ögel

Mayıs 2015, 98 sayfa

Yapılan çalışma kapsamında modifiye edilmiş AISI 4340 çeliğinin karakteristik ve mekanik özellikleri incelenmiştir. Mod I kırılma tokluğu (K_{IC}) testleri hadde yönünde ve bu yöne dik olmak üzere iki yönde yapılmıştır. Yorulma çatlak ilerleme davranışı RL ve LR yönlerinde hazırlanmış numunelerde 0.1, 0.3 ve 0.5 gerilme oranı (R) değerleri için sabit genlikli yükleme metodunda gerçekleştirilmş ve elde edilen sonuçlar kıyaslanmıştır. Pozitif R değerleri için malzeme yorulma ömrü hesaplarında Walker Denklemi kullanılmıştır. Bunu takip eden adımda, R= -1 tam ters gerinimli yükleme için deneyler yapılmış, elde edilen tüm datalar Paris-Erdoğan denklemi ile de incelenmiştir. AISI 4340 çeliği ile modifiye edilmiş M4340 çeliğinin üretim adımları karşılaştırılmış ve aradaki farkların çelik yapısına olan etkisi değerlendirilmiştir.

Yapılan deneyler neticesinde M4340 çeliğinin sertlik ve mekanik özelliklerinin AISI 4340 standart çeliğine kıyasla geliştirildiği gözlenmiştir.

Anahtar Kelimeler: AISI 4340 çeliği, Yorulma, Mode I yorulma çatlağı ilerleme hızı, Walker denklemi, Düşük karbonlu çelik.

To My Precious Family…

ACKNOWLEDGEMENTS

I would like to thank my advisor Prof. Dr. Rıza Gürbüz for his great support, encouragement and guidance throughout the whole time I have worked on this study. I would also like to express my gratitude to Prof. Dr. Bilgehan Ögel for giving me his suggestions and comments throughout the whole research. I feel so lucky to have met those great advisors and have the opportunity to work with them.

I am deeply thankful to my lab-mate Ali Motameni Tabatabaei for his infinite support and patience. The technical assistance of Mr. Cemal Yanardağ, Mr. Servet Şehirli and Mr. Önder Şahin was quite substantial.

I also appreciate the great moral support and insight from my managers and workmates Canan Onat, Selma Kara, Bahar Bikmen, Burcu Vidinlisan and Ferhat Bayrak from Havelsan Technology Radar A.S..

Finally; I would like to thank my mom, dad and lovely sister for their infinite love and support over my whole life. They are the best and I owe so much to them. Thank you for everything...

TABLE OF CONTENTS

LIST OF TABLES

TABLES

LIST OF FIGURES

FIGURES

CHAPTER 1

INTRODUCTION

Steels are widely used in areas such as automotive, construction, transportation, defense, energy and many other for long years. Since the application areas are that important and wide, many researches have been focused on steel structures. Besides classical steel types, many contemporary structures of steels are manufactured commonly in recent years due to economical reasons and long-life usage availability. As a result; the steel improvement studies take non-negligible part in materials science. Compositional changes of steel individually allows notable change in mechanical properties. Furthermore; apart from traditional production techniques, tailored processes are also used since last decades and has been an important area for suitable design. For varying applications and designs, there is a wide range of suitable steel which allows safety and improved properties for usage.

The failure of engineering materials has been another important issue and research area for many years due to the increase of material variety. Since the failure of critical components of buildings or vehicles can cause catastrophic damages, the life-time prediction is quite important [37]. The fatigue life determination of a component is quite critical both in terms of user and system safety. In 1842, France-the Meudon railway accident, in 1988 the Aloha B737 accident, in 2006 the Los Angeles B767 accident are some memorable disasters caused by fatigue [1]. In order to eliminate these failures; over the last few decades, many scientists and companies focus on steel and fatigue studies.

Figure 1.1. The Aloha Airlines Boeing 737 at Honolulu International Airport, Hawaii, following the accident on April 28, 1988.

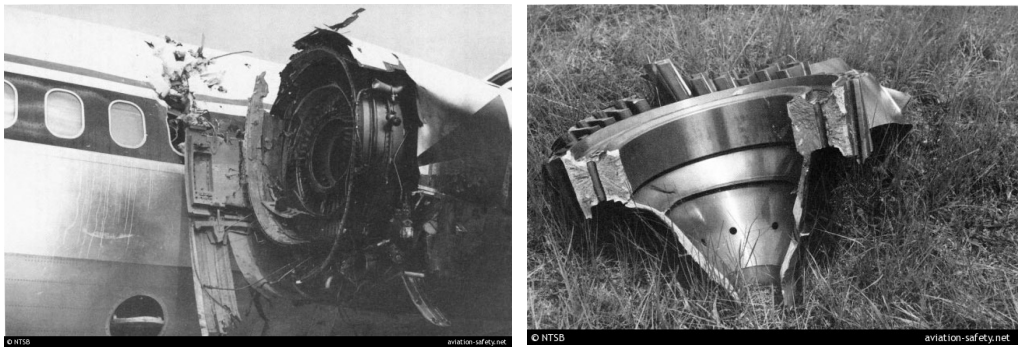

Figure 1.2. Photos of McDonnell Douglas MD-88 N927DA aircraft accident, July 6, 1996, Delta Air Lines Pensacola regional airport, Florida.

The scope of this study is to investigate the structural and mechanical properties of the received modified AISI 4340 steel (M4340) and the analysis of the interaction of each change with the properties of steel. The theoretical compositional change predictions obtained from the literature survey are achieved from experimental

studies belonging to M4340 steel. Structural improvements enable longer lifetime of the component. The improved properties such as plane-strain fracture toughness, percent elongation and hardness are peculiarly tailored for a specific application area. To sum up; by using the alloying elements and custom procedures, it is acquirable to update steel structures in an observable manner.

CHAPTER 2

LITERATURE REVIEW

2.1. STRUCTURAL FEATURES OF FATIGUE

Fatigue failures occur as a result of fluctuating stresses that are lower than the maximum stress causing failure during a single application of stress. Fatigue is an important and critical problem which can affect any part or component of the whole working system. In the early 1800's; observers have recognized that the railroad and bridge components were cracking after a period of usage due to repeated loading. Afterwards; fatigue has become an important research area. The more the usage of materials expanded and the variety has become wider, the deeper the researches take place nowadays.

Three basic factors which leads to fatigue are:
1. a maximum tensile stress sufficiently high enough,
2. a fluctuation range which has amplitude large enough,
3. sufficiently large number of cyclic loading.

There are many types of fluctuating stresses such as, fully reversed cycle, tension-tension with applied stress and random loading (Fig. 2.1). On fully reversed cycle; the mean stress is zero and the maximum and minimum stresses are equidistanced to the mean stress in positive and negative directions on the stress cycle. On random loading, the stress cycle has no continuous manner and changes simultaneously [2,31,38].

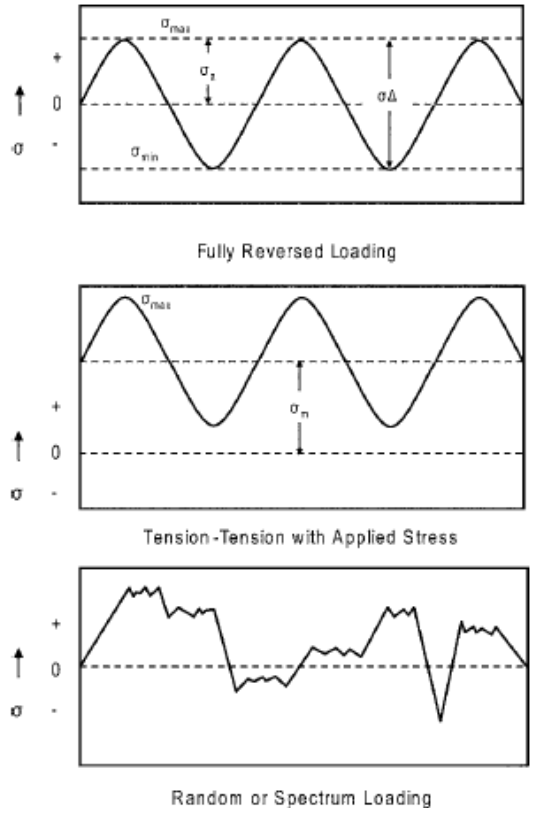

Figure 2.1. Schematic view of loading types.

Basically, a fluctuating stress has two important components, the mean stress and the alternating stress. The mean stress is the average of the sum of the maximum and minimum stress in the cycle:

$$\sigma_m = \frac{\sigma_{max} + \sigma_{min}}{2} \tag{2.1}$$

The alternating stress is the one-half of the stress range:

$$\sigma_a = \frac{\sigma_{max} - \sigma_{min}}{2} \tag{2.2}$$

$$\Delta \sigma = \sigma_{max} - \sigma_{min} \tag{2.3}$$

Besides mean and alternating stresses, there are two ratios frequently used for representing fatigue data, stress ratio (R) and amplitude ratio (A).

$$R = \frac{\sigma_{min}}{\sigma_{max}} \quad , \quad A = \frac{\sigma_a}{\sigma_m} = \frac{1-R}{1+R} \tag{2.4}$$

R = −1 represents the fully reversed loading condition. A stress cycle of R = 0.1 is generally used in aircraft component testing [42].

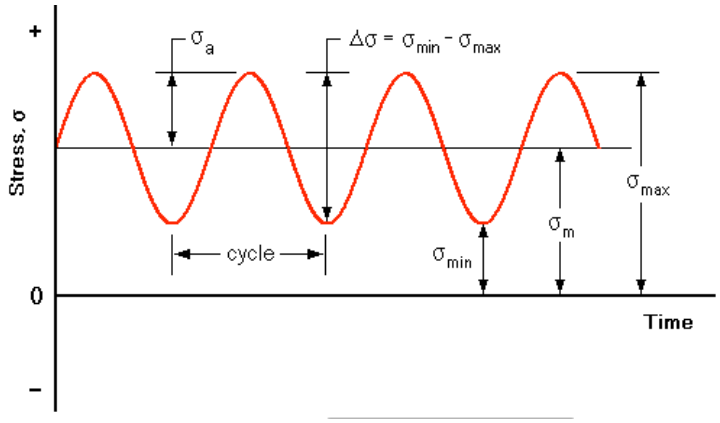

Figure 2.2. Basic terms defining constant amplitude sinusoidal loading.

When a metal is subjected to cyclic stress, structural changes and fatigue process occur. For easier examination, fatigue process can be divided into four main stages each including different mechanisms.

1. *Crack initiation stage* – In this stage, the precursor development of fatigue damage is present which can be eliminated easily by applying different thermal annealing procedures.

2. *Slip-band crack growth stage* – On this stage, the growth of the initial crack on the planes of high shear stress occurs. This stage is mainly described as *stage I crack growth.*
3. *Crack growth on planes of high tensile stress stage* – This stage includes the growth of crack in normal direction to maximum tensile stress. This stage is mainly described as *stage II crack growth.*
4. *Ultimate ductile failure stage* – is the final stage where the crack reaches to critical length therefore; the material can not resist the applied load anymore. As a result of this stage, failure is observed.

The number of cycles contributing each stage changes due to the loading conditions and material properties. Stage I crack growth may not be observable if the tensile stress is high.

In order to understand the reasons and effects of fatigue mechanism, W. A. Wood made many investigations. In 1950's, he had conducted a microscopic observation of slips produced by fatigue and indicated that the slip bands are produced of systematic buildup of fine slip movements on the order of 1 nm rather than steps of 100 to 1000 nm as seen on Figure 2.3 [3, 31, 33]. As a result of back-and-forth fine slip movements of fatigue, notches or ridges can be build up at the surface of the metal. The notches act as stress raisers and become the start of a fatigue crack.

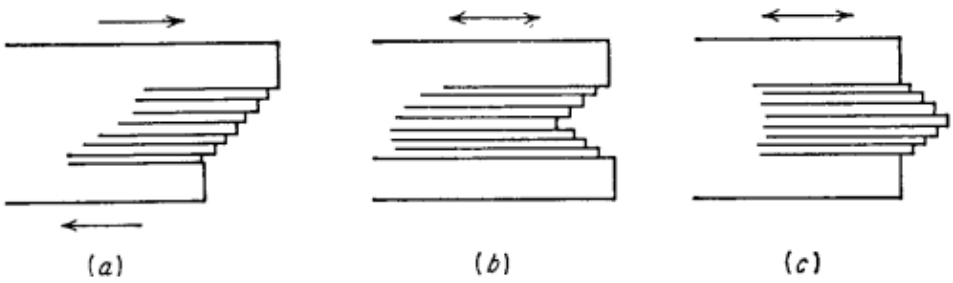

Figure 2.3. W. A. Wood's model for fatigue crack initiation.

In stage I, the crack propagates along the persistent slip bands in a polycrystalline metal. The crack may extend for only a few grain diameters before the crack propagation changes to stage II. The crack propagation rate is found to be very low for stage I when compared with the rate in stage II.

Stage II crack propagation occurs by a plastic blunting process which can be seen on Figure 2.4. At the beginning of the loading cycle, the crack tip is sharp (Fig. 2.4.1). As the tensile load is applied the small double notch at the crack tip concentrates the slip along planes at 45° to the plane of the crack (Fig. 2.4.2). As the crack widens to its maximum extension (Fig. 2.4.3) it grows longer by plastic shearing and at the same time its tip becomes blunter. When the load is changed to compression the slip direction in the end zones is reversed. The crack faces are crushed together and the new crack surface created in tension is forced into the plane of the crack (Fig. 2.4.5) [4].

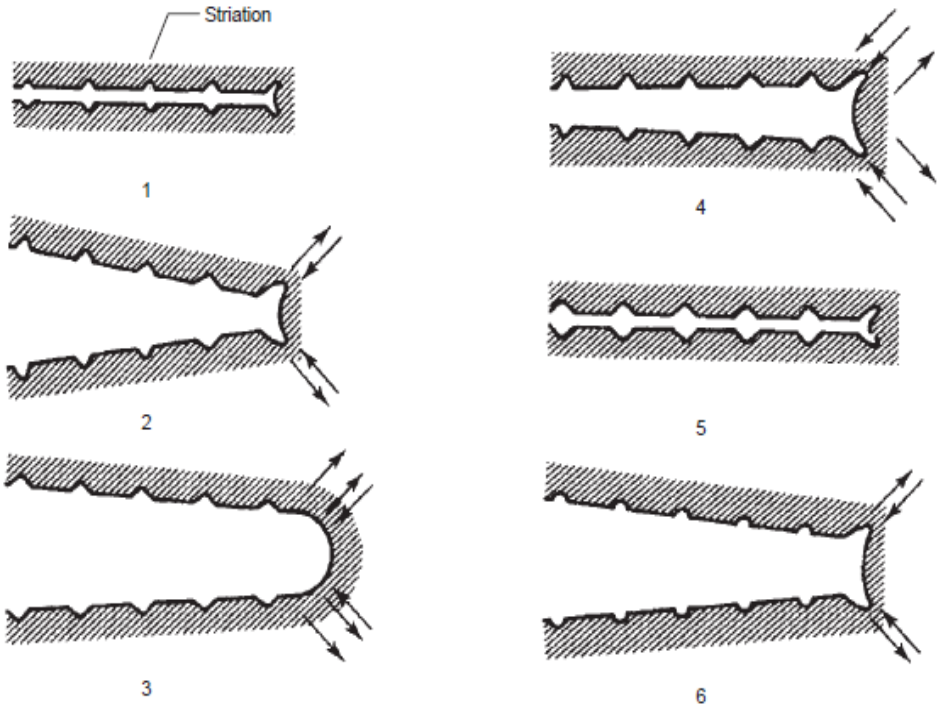

Figure 2.4. Plastic Blunting process for stage II crack propagation.

Fracture modes can be divided into 3 main groups which can be seen schematically on Figure 2.5. The loading direction and the material's response has been taken into consideration in the classification. The mode I (*opening mode)* represents the case that the material is loaded by tensile forces on y direction and crack surfaces are pulled apart in the same direction. In mode II (*sliding mode*), the material is loaded by shear forces which are parallel to the crack surfaces. The crack surfaces slide over each other on x direction. In mode III (*tearing mode*), the material is loaded by shear forces on z direction. The crack surfaces slide over each other in the loading direction.

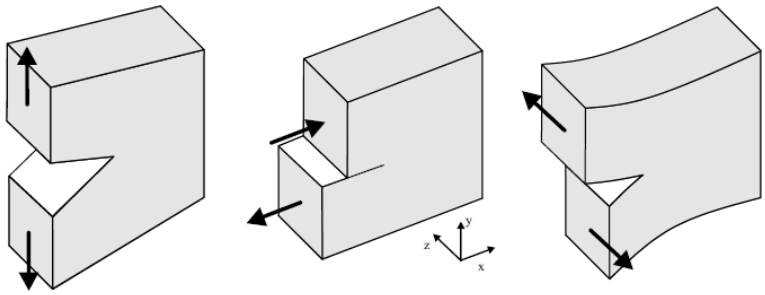

Figure 2.5. Modes of fracture a. Mode I b. Mode II c. Mode III.

2.2. FATIGUE CRACK PROPAGATION

In fail-safe design, crack growth rate versus stress intensity factor range curves are quite important since they give the stable crack growth region which can be controlled. The estimated service life of a component allows us to avoid unpredictable failures of huge systems. Different theories have been studied over years in the analysis of crack formation and failure such as Griffith, Irwin, Tada and Paris, etc. [36].

The obtained crack length (a) versus number of cycles (N) curves are analyzed in order to obtain fatigue life information about the material and fatigue crack growth behaviour. The discussion due to the results are quite important for damage tolerant design. ASTM E647 standard gives the method for determination of stress-intensity factor range (ΔK) for compact tension C(T) specimens as below [5].

$$\Delta K = \frac{\Delta P}{B\sqrt{W}} \frac{(2+\alpha)}{(1-\alpha)^{\frac{3}{2}}} (0.886 + 4.64\alpha - 13.32\alpha^2 + 14.72\alpha^3 - 5.6\alpha^4) \qquad \textbf{(2.5)}$$

where, $\alpha = a/W$. The expression is valid if only $a/W \geq 0.2$.

On Figure 2.6, a typical crack growth rate versus stress intensity factor curve is given. Basically, the crack growth process can be divided into 3 regions. The first region is the place where there is no crack growth. In the second region, there is a linear relationship between the crack growth rate and ΔK**.** Therefore; second region is told to be the linear or the stable crack growth region. On the final region, the crack growth is rapid and unstable which leads to failure at the end.

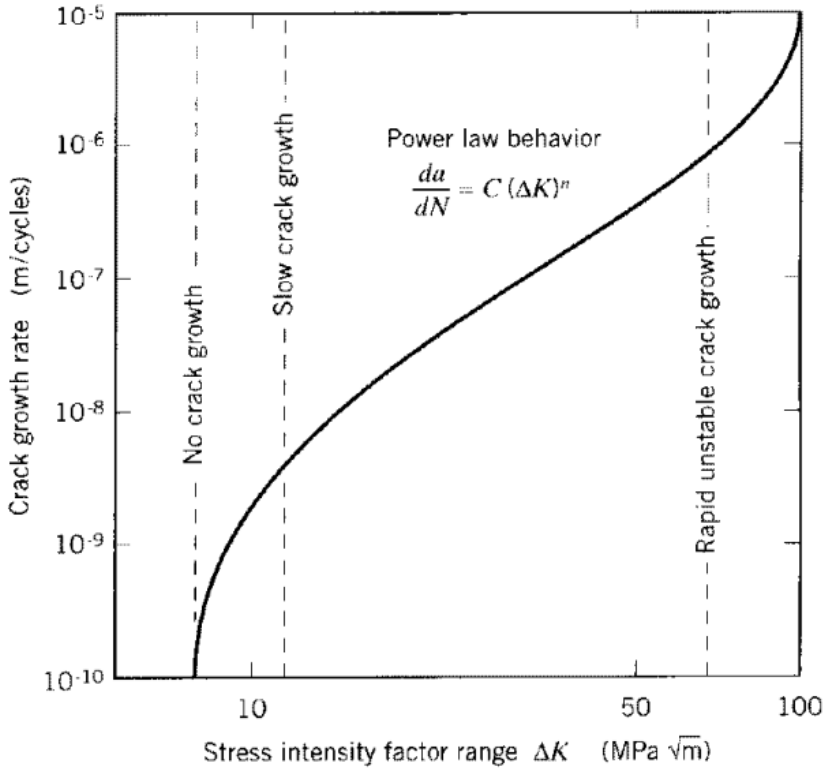

Figure 2.6. Typical crack growth rate versus ΔK curve.

One of commonly used theory about fatigue crack growth region II is Paris-Erdogan Law. In 1963, Paris and Erdogan proposed the empirical relation equation 2.6 below.

$$\frac{da}{dN} = C.(\Delta K)^n \tag{2.6}$$

There are some deficiencies of Paris law which is not well-described. First of all, it is non-conservative. Since it does not take the quite fast and unstable region III into consideration, the number of cycles for failure is overpredicted. Therefore; the predicted lifetime for material is rough and not well-fitted to the real service conditions. Secondly; the model fails for nonzero R values. Since the law does not

include the effect of stress ratio (R), a separate calibration curve should be fitted for each load ratio which means a waste of time and an inadequate approach.

In 1970, Walker proposed another crack propagation model in the form of

$$\frac{da}{dN} = C(\Delta K_{eq.})^n \tag{2.7}$$

where, $\Delta K_{eq.}$ is the new term defined including stress ratio inside.

$$\Delta K_{eq.} = \frac{\Delta K}{(1-R)^{(1-m)}} \tag{2.8}$$

in order to incorporate the effect of stress ratio into the Paris model. One additional degree of freedom is introduced into calculations by Walker [44, 45]. Since an important variable stress ratio R is included in all calculations, Walker Equation can told to be more precise compared to Paris-Erdogan Law.

Different data reduction methods can be used in the reduction of fatigue crack growth test data. Below, a brief summary of some frequently used techniques is given.

- Mukherjee proposed a model of calculating finite differences between successive data points and making a linear interpolation in order to estimate the gradient at the mid-point [6].
- Smith fitted the best smooth curves to the test data and took gradients of the slope [7].
- Davies et al. fitted an analytical curve, such as polynomial, to all data or a part of it [8].
- Munro proposed to use orthogonal polynomial method to fit cubic expressions to equidistantly placed crack lengths [9].

- Polak et al. used spline technique in data smoothening and interpolation [10].
- Another method is the incremental polynomial method in which a second-order polynomial is fitted to sets of (2n+1) successive data points where n is usually 1, 2, 3 or 4 [5].

Over all techniques, the best one which gives the most accurate result is the incremental polynomial method which includes differentiation to obtain crack growth rates. On the related ASTM standard, the seven point incremental polynomial method is also selected as the effective data reduction method. This method can be told to be a little time consuming but it is worth to use it and evaluate test data with [11,12]. In order to minimize the square of the deviations between the test data and fitted values (least squares method), consecutive sets of seven successful data points are used. The crack growth rates are obtained from the first derivative of the fitted curve's equation.

Second order incremental polynomial method defines two constants which are C_1 and C_2 and relates them with a_i term as given below.

The validity requirement of $\left(\frac{N_i - C_1}{C_2}\right)$ should be satisfied for correct analysis.

$$a_i = b_0 + b_1 \left(\frac{N_i - C_1}{C_2}\right) + b_2 \left(\frac{N_i - C_1}{C_2}\right)^2 \qquad \textbf{(2.8)}$$

where; $-1 \leq \left(\frac{N_i - C_1}{C_2}\right) \leq 1$ and.

$$C_1 = \frac{1}{2}(N_{i-n} + N_{i+n}) \quad , \quad C_2 = \frac{1}{2}(N_{i+n} - N_{i-n})$$

$$\frac{da}{dN} = \frac{b_1}{C_2} + \frac{2b_2(N_i - C_1)}{C_2^2} \qquad \textbf{(2.9)}$$

In order to find the Stress-Intensity Range (ΔK), $\hat{a}_i$ is placed in the formula of ΔK given below.

$$\Delta K = \frac{\Delta P}{B\sqrt{W}} \frac{(2+\alpha)}{(1-\alpha)^{3/2}} (0.886 + 4.64\alpha - 13.32\alpha^2 + 14.72\alpha^3 - 5.6\alpha^4) \quad \textbf{(2.10)}$$

2.3. THE EFFECT OF MEAN STRESS

Structural components in service subjected to cyclic loads exhibit a fatigue behaviour that mostly depends on the mean stress values and an increase in mean stress causes a reduction in fatigue life. Therefore; the effects of mean stress have been an important issue for long years and many empirical relations have been developed [46].

Generally, fatigue testing includes a mean stress of σ_m on which a sinusoidal cycle is superimposed as shown in Fig. 2.2. Such a cycle can be described by using alternating stress (σ_a) and stress ratio (R) as mentioned above. S-N fatigue curves are influenced by stress ratios in such a manner that, as the mean stress increases, the fatigue lifetime decreases as seen on Figure 2.7.

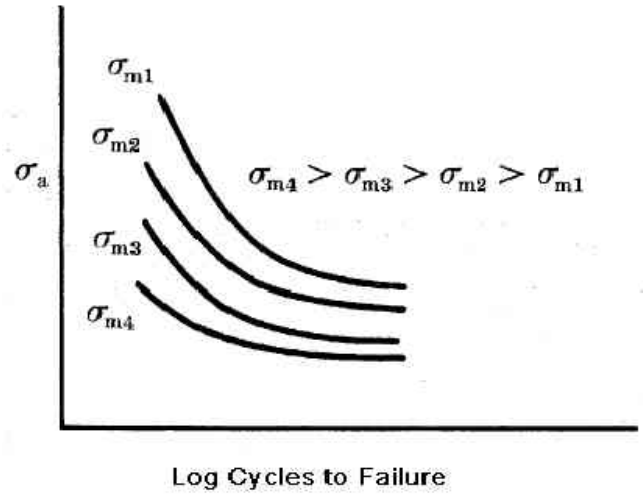

Figure 2.7. Demonstration of the influence of mean stress (σ_m) on S-N curve.

Different mathematical models have been developed that allows prediction of fatigue life given in Figure 10. Goodman (1899) had developed a linear model, while Gerber used a parabolic model (1874). Besides these two models, Soderberg had introduced a new model for the case that the component design is based on yield stress rather than ultimate stress on 1939. Life predictions based on the Soderberg mean stress criterion are conservative while Gerber criterion based life predictions are non-conservative [13, 14, 15, 42, 53].

$$\sigma_a = \sigma_e \left[1 - \left(\frac{\sigma_m}{\sigma_u}\right)^x\right] \quad \textbf{(2.11)}$$

where x=1 for Goodman line, x=2 for Gerber curve, $\sigma_u = \sigma_y$ for Soderberg curve and σ_e is the fatigue limit for completely reversed bending.

The lines on Figure 2.8 are determined experimentally from S-N curves for different load ratio values and refer to combinations of alternating and mean stresses that have

the same endurance limit. As expected, the higher the mean stress, the lower the alternating stress which has the same lifetime [53].

Figure 2.8. The mean stress effect on fatigue life: Soderberg, Goodman and Gerber criteria.

2.4. THE BASIS OF STRAIN GAGE

Among all of the experimental techniques used in the analysis of fracture mechanics; the most commonly used and well developed is the usage of electrical resistance strain gages. Basically, a strain gage is a strain sensitive pattern which consists of an electrical wire and terminals. In tension condition, the area of the gage and the wire narrows and as a result the resistance increases. In compression condition, the area of the gage and the wire thickens and the resistance decreases.

$$R = \frac{\rho L}{A} \tag{2.12}$$

where; ρ is resistivity, L is length and A is the cross-sectional area of the wire.

A strain gage which can be seen on Figure 2.9, is considered to be located at an arbitrary point (r, θ) relative to the crack tip with an oriented gage at an angle of α.

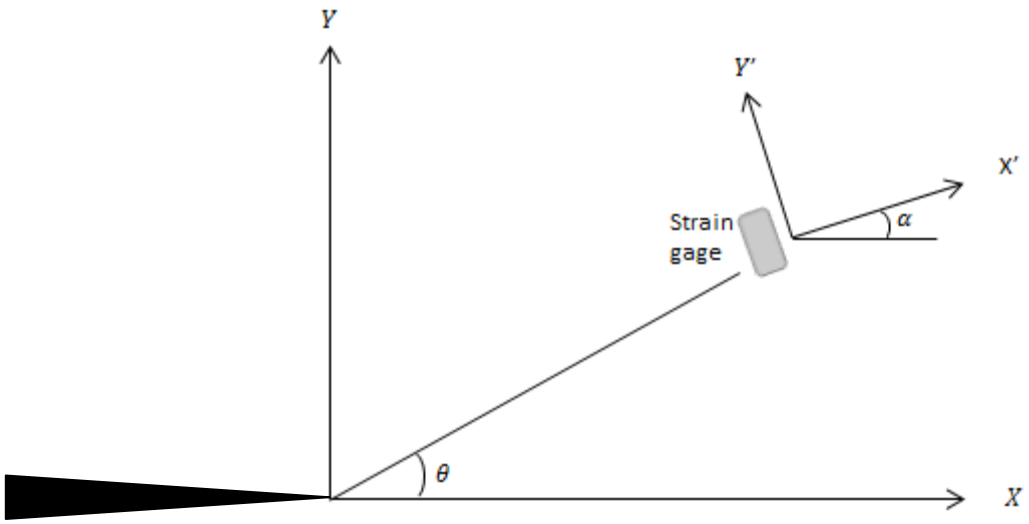

Figure 2.9. The location and orientation of a single strain gage relative to the crack tip.

$$K_I = E\sqrt{2\pi r}\epsilon_{x'x'}f(\gamma) \qquad \textbf{(2.13)}$$

where $f(\gamma)$ is a function of α, the gage rotation angle and θ. The location and orientation of the gage affects $f(\gamma)$.

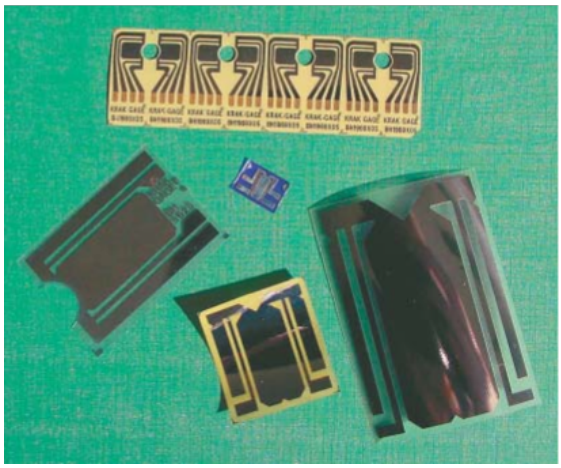

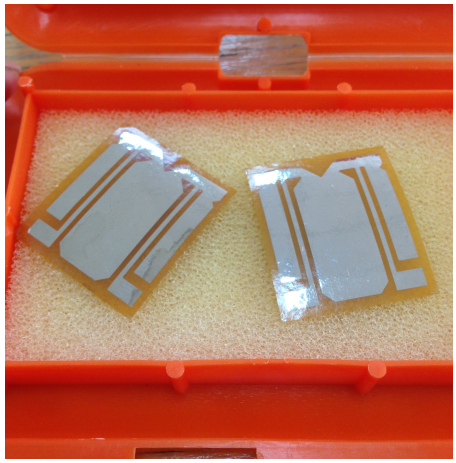

Figure 3.10. Various crack gages by Rumul.

2.5. HEAT TREATMENT OF STEELS

All heat treatment procedures are composed of a heating step, holding at an elevated temperature for a period of time and consequently, cooling. The time spent at each step may vary due to the application area of steel and the required resultant structure. The heating-cooling rates and temperature ranges are determined due to the Time-Temperature-Transformation (TTT) and continuous cooling transformation (CCT) curves of the metal [27].

By holding the steel at an elevated temperature, heat uniformity is aimed to be achieved over the entire volume. Moreover; changing quenching media directly affects the structure and properties [43]. As the section gets thicker, the cooling rates will be slower regardless of the cooling method except some techniques such as induction hardening [39, 40].

"Full annealing" is a basic softening process in which the steel is heated up to a temperature above its transformation range, held at this temperature for a period of time and finally cooled controlly above its critical transformation range. The steel can either be held at a furnace for cooling or a media can be used for treatment.

"Normalizing" is another process where the steel is heated up to an elevated temperature above A_{c3} or the A_{cm} and cooling consequently in air. The basic aim of normalizing treatment is to eliminate the effects of previous heat treatments and to obtain a more homogeneous structure.

Another important process is "tempering" which is basically reheating the steel structure to some temperature below the lower critical $A_{c1.}$ As mentioned above, tempering temperatures are also determined due to the desired properties and the application area of the steel. If there is a requirement for improved hardness, the tempering temperature should be low whereas; the tempering temperature should be high if improved toughness is required [16, 41, 48].

2.5.1. ELECTROSLAG REFINING

Electroslag refining (ESR) is a secondary refining process for metals used over years, which has already been well established for producing high quality steels and other high quality alloys [17,18,19].

In the process, an electric current flowing between an anode and a baseplate is used in the melting procedure of the steel. The electrode is fed into the slag bath and as the temperature of the slag bath increases, metal melts and as a result droplets of molten metal fall through the slag and collected on the baseplate for solidification. At the end, refining is achieved due to the reaction between the metal and the slag [18, 19, 20].

2.5.2. VACUUM DEGASSING

During steel making gases like oxygen, hydrogen and nitrogen dissolve in steel. They can be present in the structure either in the form of molecules or elements. Oxygen and hydrogen are mainly some of the most important elements in steel structure which can not be removed since it occurs in molecular structure. Initially, vacuum degassing was used a few decades ago for hydrogen removal from the steel structure which causes embrittlement in later stages of processing or application. Since then; vacuum degassing procedure is commonly used for critical steel applications in order to eliminate hydrogen and oxygen which can lead to failure.

Degassing effectively prevents this low ductility from occurring and provides more precise steel structure. Since the vacuum degassing setup and procedure is not a low-cost one; generally special application oriented steels are subjected such as aerospace and defense applications.

During the Vacuum Degassing treatment, the liquid steel ladle is placed in a vacuum tank that can be either stationary or movable due to system design. By using a suitable vacuum pumps, vacuum is achieved in the system. Inert gases are used in order to stir the melt and remove undesired structures.

Some Advantages of Vacuum Degassing technique can be listed as below:

- By using high vapor pressures, undesired trace elements can be eliminated.
- Dissolved gases such as oxygen, hydrogen, nitrogen can be removed.
- Melting in an oxygen-free atmosphere prevents the formation of non-metallic oxide inclusions and inhibits oxidation.
- The alloy composition can be adjusted precisely and homogeneous alloy composition can be achieved [51].

CHAPTER 3

EXPERIMENTAL PROCEDURE

3.1. MATERIAL PRODUCTION STEPS

In order to tailor the properties of 4340 steel, electroslag refining (ESR) and vacuum degassing are probably used on manufacturing steps besides compositional changes. Since the application area of the steel is critical and important, ESR and vacuum degassing are the commonly used techniques and helps to improve the properties by refining steel structure by eliminating non-metallic inclusions before final heat treatment.

The temperature ranges, heating/cooling rates and cooling ambient on Figure 3.1 are chosen to obtain maximum toughness with smaller available grain size. The main aim of choosing and applying these steps are;

- To improve machinability,
- To eliminate residual stresses,
- To improve formability,
- To improve mechanical properties,
- To obtain homogeneous structure.

The very coarse sizes can be obtained if only the large steel ingots are held near their melting points for long times [21]. Special heat treatment steps are taken into consideration in order to inhibit grain growth and obtain finer grain structures.

Hall-Petch equation given below represents the relationship between yield stress and grain size diameter. As can be seen, the smaller the grain size, the higher the yield stress can be obtained.

$$\sigma_y = \sigma_0 + \frac{k}{\sqrt{d}} \quad \textbf{(3.1)}$$

where;

σ_y: yield stress at average grain diameter d,

σ_0: friction stress,

k: empirical constant, locking parameter (relative hardening contribution of grain boundaries)

d: average grain diameter [22].

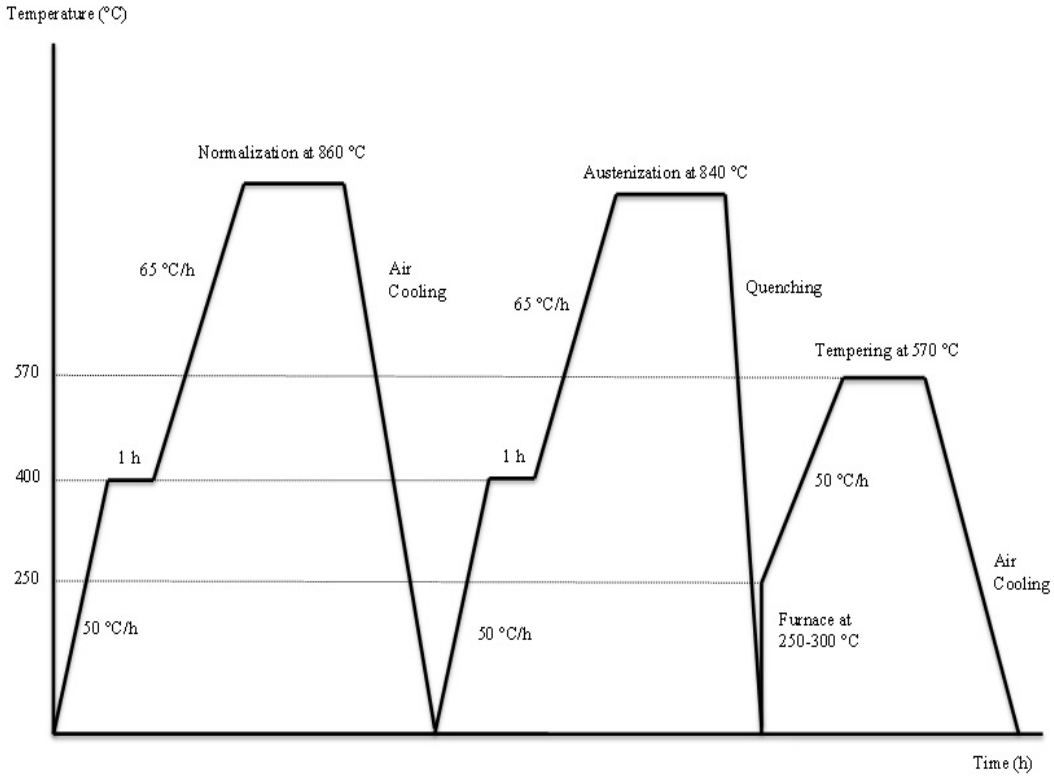

Figure 4.1. Heat treatment steps applied in the production of M4340 steel.

The sectional temperature increase including 400 °C steps were selected and applied in order to minimize the distortion in the material. The material was held at 400 °C for 1 hour therefore; the continuous heating was divided into two parts.

On normalization step, steel was heated up approximately 60 °C above its critical temperature and then cooled with air. As a result; microstructure becomes more homogeneous, grain structure gets smaller and the residual stresses are eliminated.

Austenisation step takes 6 hours and compared to the study of Miller, it is a long period of time [23]. When dealing with hypoeutectoid steels, in order to reduce grain size and obtain finer structure, the pearlite steel should be heated up into 100% austenite region and the maximum temperature should be kept as low as possible while the molten steel should be cooled with air as fast as possible to room temperature [22].

On the quenching step, the pressure of water was 2.8±0.2 bar. The M4340 steel billet was rotated with a speed of 20-30 turns/min. After quenching step, the material obtained is brittle with improved toughness and includes inherent stresses due to fast cooling. Therefore; tempering step is widely used in steel production.

When austenite is rapidly cooled by quenching, martensite can appear besides bainite. Martensite grows very fast and is a non-equilibrium phase (it does not appear on the phase diagram). The more carbon in austenite phase, the harder and stronger the martensite and the steel is. Since martensite structure is formed at slow cooling rates, the alloying elements increase the depth below the surface where 100% martensite forms at a quenched bar. Therefore; the hardenability is said to increase as a result. Bain et al. expressed on their study the effect of various transformations on hardness and it is found to be that the hardness of martensitic structure is approximately 5 times of the hardness of air cooled pearlitic structure [24].

As tempering temperature rises, the fine carbides gets bigger-coarsen and reduce

their strengthen contribution. The addition of Cr and Mo slows down the coarsening of carbides, as a result, an improvement in strength and hardness can be obtained after tempering.

If the maximum treating temperature is kept as low as possible and the heating and cooling processes are kept fast enough, the reduction in grain size can be improved.

3.2. SPECTRAL ANALYSIS

The received specimen was prepared for spectral analysis and has been examined. The chemical composition was found to be as shown in Table 3.1. Compared to ASTM DS76A standard values; Mn, P, S are lower and Cr, Mo, Ni are higher in weight percent in low-alloy steel.

Table 3.1. Chemical composition comparison of M4340 steel and AISI 4340 steel in weight percentages due to ASTM DS76A standard.

	C	Si	Mn	P	S
M4340	0.4132	0.2471	0.2461	0.0043	0.0049
AISI 4340	0.38-0.43	0.15-0.35	0.60-0.80	0.035	0.040

	Cr	Mo	Ni	Cu	Al
M4340	1.1552	0.4666	2.2247	0.1785	0.0106
AISI 4340	0.70-0.90	0.20-0.30	1.65-2.00	0.35	

	Nb	V (max)	W (max)	Pb (max)	Bi (max)
M4340	0.0022	0.0686	0.0002	0.0002	0.0002

	Sb	B	N	Fe
M4340	0.0006	0.0009	0.0117	94.9645

The critical temperatures can be shown on Figure 3.2 -metastable Iron-Carbon phase diagram due to spectral analysis compositional results. The red line on the figure represents M4340 steel with 0.4132 wt % C.

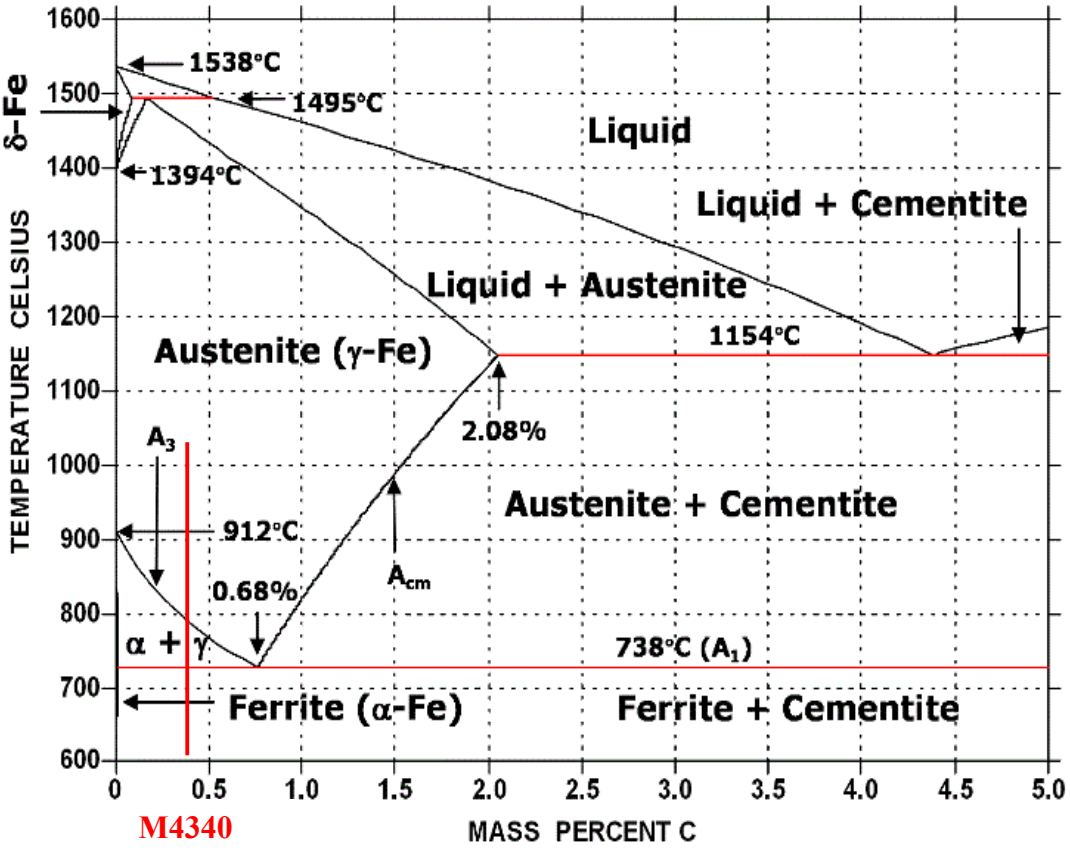

Figure 3.2. Metastable Iron-Carbon Phase Diagram.

The hardenability or hardening depth of steel can be developed with the help of the increase in the particle size of austenite thanks to carbon fraction or addition of alloying elements. In order to increase the hardenability of the steel, alloying elements can be introduced to decrease the critical cooling rate and so facilitates formation of martensite. Moreover, if the proportion of the carbon in steel increases, the formation of the martensite goes up, as well. Owning to the condition, resistance of steel to tension and hardening can be doubled [25].

3.3. METALLOGRAPHY

In order to conduct metallographic examinations, samples were cut from the center and surface region of the billet. To begin with, emery papers with grade of 180, 220, 400, 600 and 800 were used respectively for grinding. On the next step; diamond polish of 6K and 1K were used and subsequently etched with 0.2% nitric acid. Finally, the specimens were cleaned with alcohol to observe the complete microstructure under optical microscope and SEM examinations. Olympus optical microscope and METU METE NOVA NANOSEM 430 scanning electron microscope were used for metallographic examinations.

3.4. MECHANICAL TESTS

3.4.1. TENSILE TEST

The tensile test specimens of M4340 steel in transverse direction which are machined due to TS EN ISO 6892-1 Standard [26] shown on Figure 3.4 were examined on the Instron 5582 tensile-compression test machine in order to determine the behavior under a tensile force of 10 kN at room temperature using a strain rate of 2 mm/min (Figure 3.5).

The specimen configuration is given below on Figure 3.3 where;
d_0: initial body diameter.
L_c: body length.
L_0: initial measurement length.
L_t: total length of the specimen.
S_0: cross-sectional area of the body symbolizes the initial dimensions.

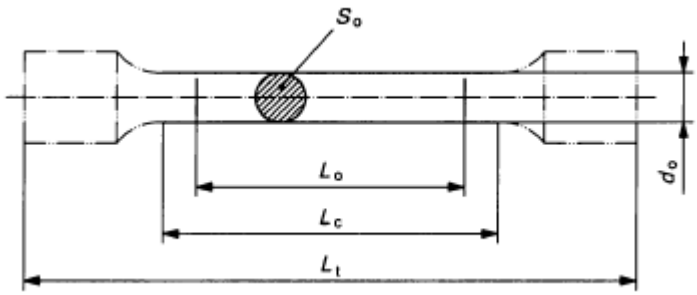

Figure 3.3. Tension Test specimen configuration.

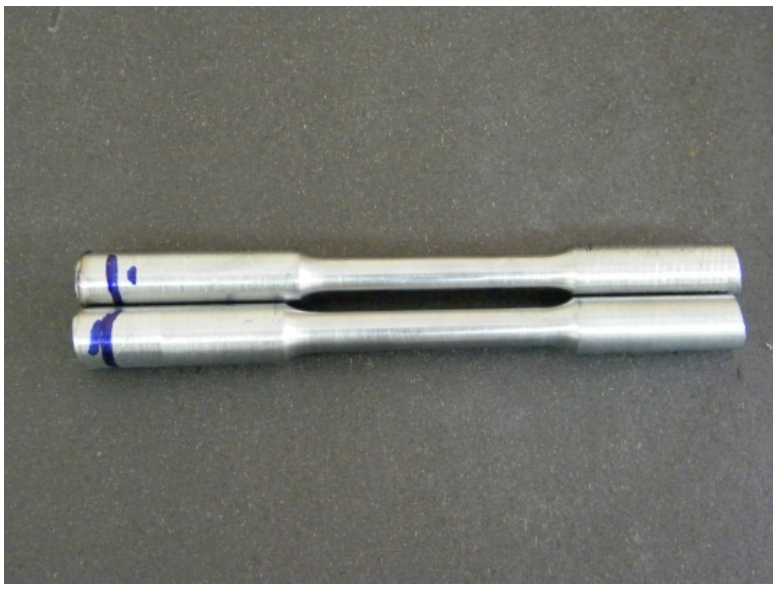

Figure 3.4. Tension test specimens machined for Instron.

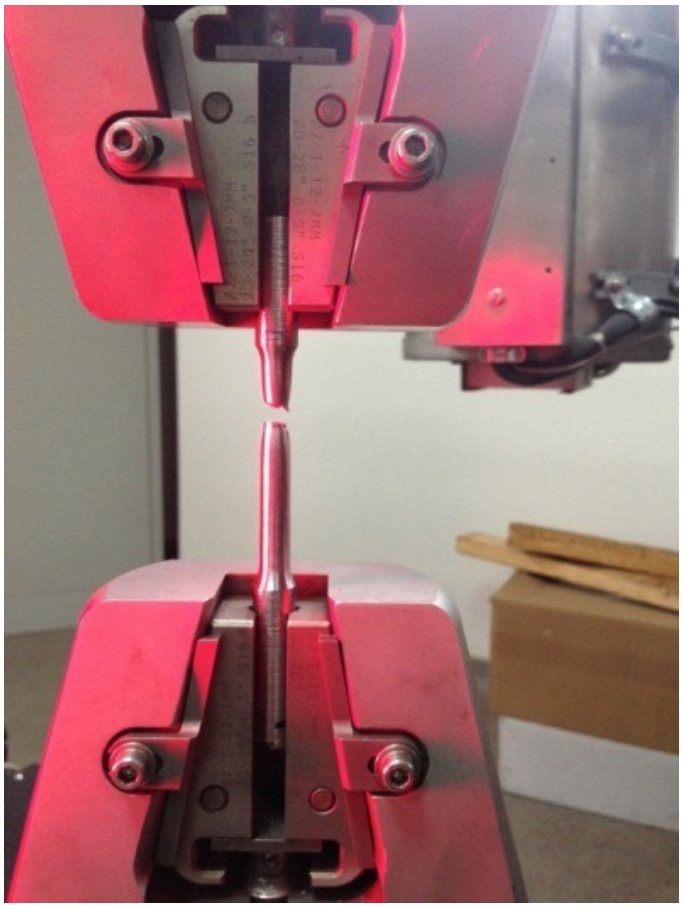

Figure 3.5. Tension Test equipment Instron 5582.

3.4.2. CHARPY IMPACT TEST

Due to related standard ASTM E23-12c [28], the specimens were machined as 4 sets each including 2 specimens from transverse direction having notches parallel to the rolling-longitudinal direction (Figure 3.7). For four different temperatures; room temperature, 0 ^{o}C, -20 ^{o}C and -40 ^{o}C; the Charpy Impact tests were conducted on Tinius Olsen pendulum impact tester having the capacity of 358 J. in Machine Shop of METE METU. The absorbed energy values are recorded for each set.

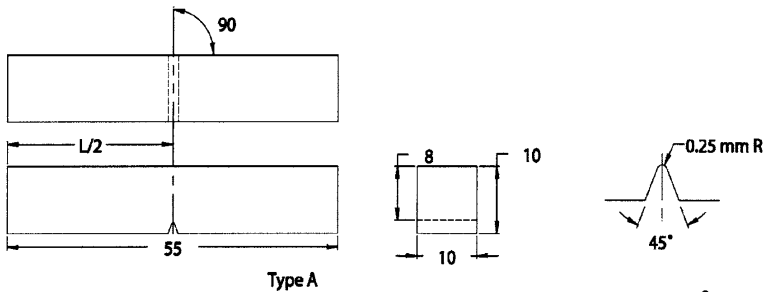

Figure 3.6. Schematic view of Charpy Impact Test specimen.

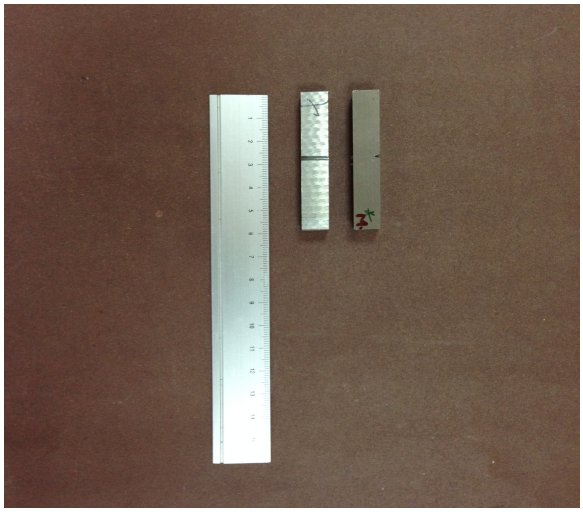

Figure 3.7. Charpy Impact V-notched Test specimens.

3.4.3. HARDNESS TEST

In order to determine the hardness of the specimen, an 18 cm diametered disc has been cut from the billet and prepared for Brinell Hardness Test. The tests were conducted on Universal Emco M4U-025 machine belonging to Machine Shop of METE METU with respect to the related standard of ASTM E10-12 [29]. A tungsten

carbide ball indenter of 2.5 mm diameter applied 187.5 kg for 15 sec. in the analysis. Since the specimen was round sectioned, the left and right regions of the center point are assumed to be in the same structure and hardness profile. Therefore; by using inductive method, the whole hardness profile is achieved.

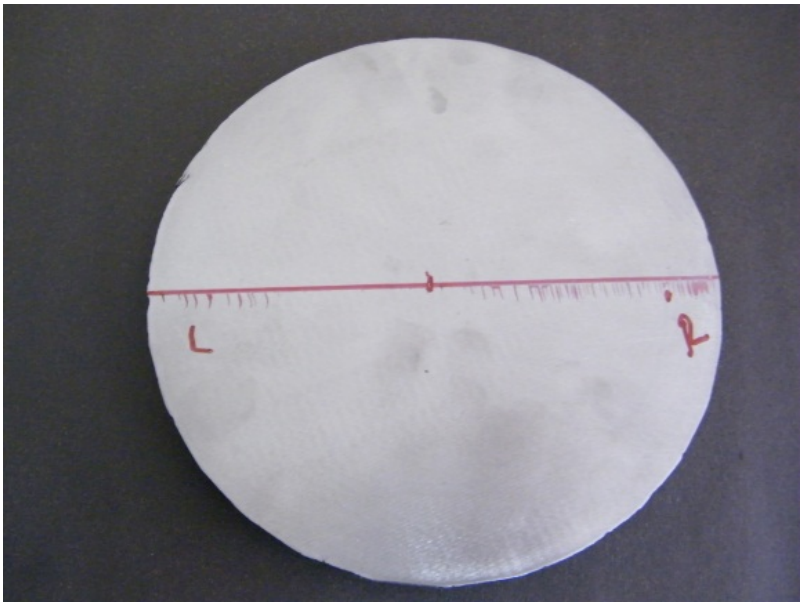

Figure 3.8. Brinell Hardness test specimen.

3.4.4. PLANE-STRAIN FRACTURE TOUGHNESS TEST

In plane-strain fracture toughness test, crack mouth opening displacement (CMOD) and force data is required to conduct analysis. This data can be taken by the help of a computer data acquisition system. To record the crack mouth opening displacement, a displacement gage is required. Thus, a displacement gage was mounted to the specimen via integral knife edges. The distance between the integral knife edges is 12 mm because of the working range of the displacement gage available.

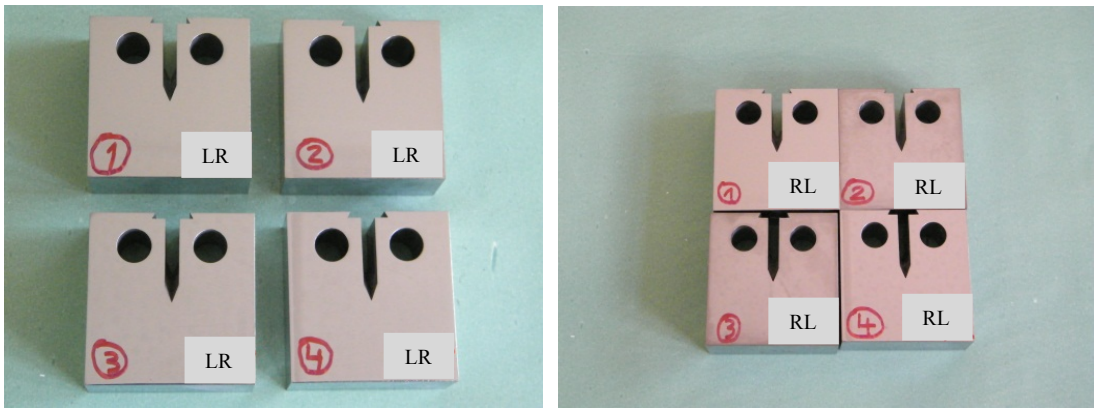

Figure 3.9. Plane-Strain fracture toughness specimens.

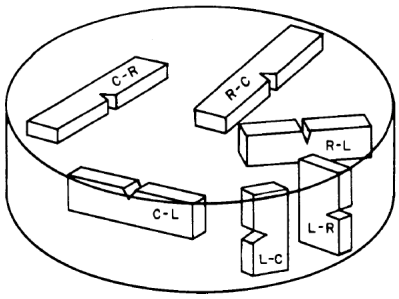

Figure 3.10. Crack Plane Orientation Code for Bar and Hollow Cylinder.

The machined specimen (Figure 3.9) suitable for the related standard ASTM E399 [50] is tested on MTS 810 universal servo-hydraulic system. Sinusoidal waves with R=0.1 are applied and thus, the specimens are subjected to fatigue cycling. First of all, a precrack is introduced by using a load which does not exceed the 80% of the predicted K_{IC} value in order to avoid sudden failure and/or unobservable quite high rate of fatigue crack growth. A traveller microscope with a precision of 0.1 mm is used for observation of the precrack until it reaches 0.5W. On the next step, the displacement gage MTS 632.01 is attached to the integral knife edges as shown on Figure 3.11 and the specimen is loaded with a load having rate of 0.5 kN/s until

fracture occurs. The applied force versus crack mouth opening displacement (CMOD) data was recorded for 4 pieces of LR and RL directional specimens.

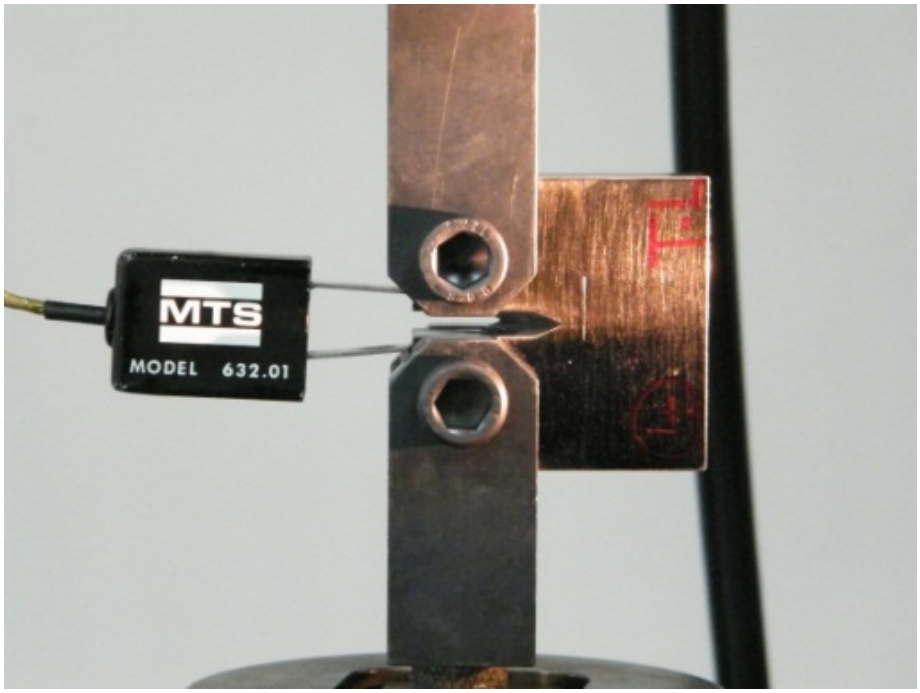

Figure 5.11. Displacement gage attached to the specimen.

3.4.5. FATIGUE CRACK GROWTH RATE TEST

3.4.5.1. FATIGUE CRACK GROWTH RATE TEST SPECIMEN

The C(T) compact tension test specimens from LR and RL directions were machined due to ASTM E647 standard configurations [5].

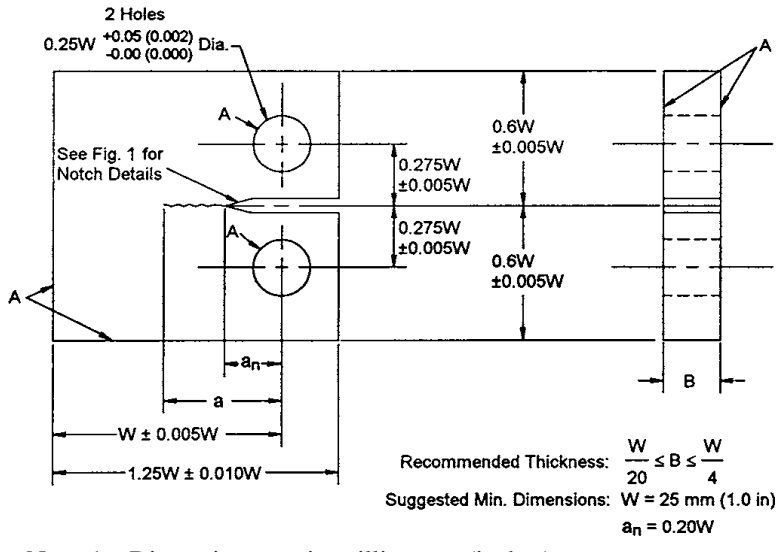

Figure 3.12. The configuration of compact tension C(T) specimen for fatigue crack growth rate testing due to ASTM E647 standard [5].

Crack length foils, trade marked as Krak Gage by Rumul Company, were used during the experimental steps of determining the crack growth rates. Among many proper crack gages with different sizes, B20 gage -sized 3.4 cm*3 cm- was chosen since it fits properly to the dimensions of the sample used throughout the experiments besides the availability of measuring crack lengths of 20 mm. On the precursor experiments, A10 crack gages were used but since the failure of the material could not be analyzed within the gage, a bigger sized B20 crack gage became a part of the experiments. The gages were aligned due to the machined notch and then glued on to one face of each C(T) specimen by 270 Z Schnellklebstoff.

First of all, by using emery papers with grades of 220, 400 and 600 level respectively, the sample surfaces were grinded. After that, in order to eliminate the effect of contamination, sample surfaces' were cleaned with alcohol. On the next step, glue was poured on the grinded face of the sample by using a PVC spatula in

order to achieve homogenous dispersion. Finally, crack gage was placed suitably aligned with the machined notch and pressure was applied by hand with using teflon foil during 2 minutes. Afterwards, the specimen was put into a specifically designed gluing tool which ensures sample to uniform pressure distribution on crack gage in order not to allow the formation of air bubbles between the gage and sample (Figure 3.13). For 15 minutes sample was kept as pressed by gluing tool and then sample was separated from gluing tool in order to solder the electrical wires.

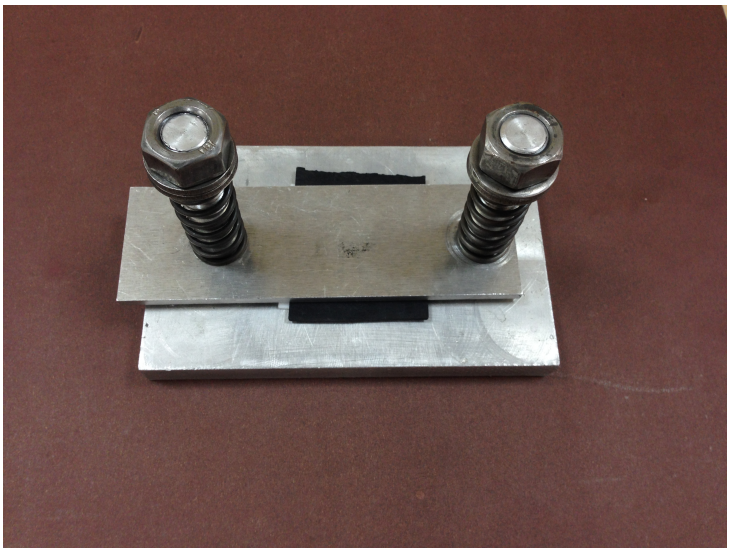

Figure 3.13. Gage implementation apparatus.

As mentioned before, two different sized gages were used in the experiments such as A10 and B20. On Figure 3.14, two specimens on which had been implemented small sized A10 crack gages are given.

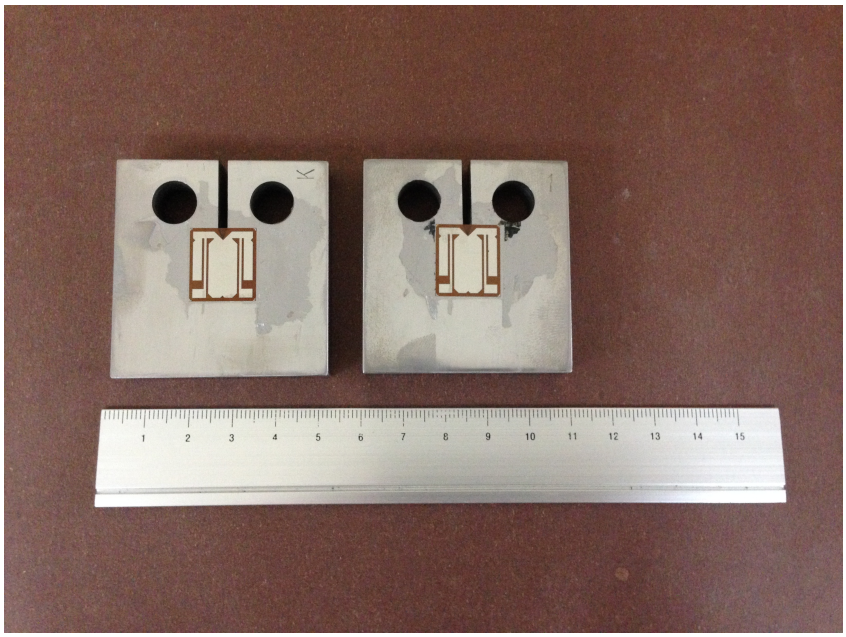

Figure 3.14. Some of the A10 gage implemented specimens.

The crack gages are thin, foil-like structures which include small electrical wiring patterns inside of them. As the material is subjected to strain and crack propagates, the wires on the foil slightly bends and electrical resistance of the wire changes. By measuring only the electrical resistance, you can get information about the propagating crack and strain occurred on the material. The electrical data obtained is transferred to a computer by using electrical cable as seen on Figure 3.15.

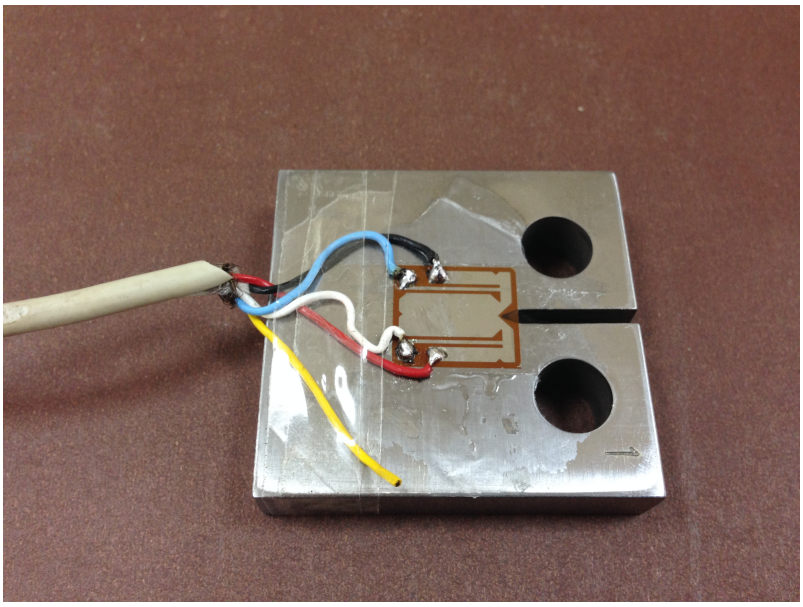

Figure 3.15. Electrical wire soldered on Gage A10 implemented on M4340-LR.

3.4.5.2. FATIGUE CRACK GROWTH TEST EQUIPMENT

The fatigue crack growth tests were conducted on a MTS 810 servo-hydraulic system with a capacity of 10 tons (Figure 3.16) due the related standard of ASTM E647 [5]. For three different positive stress ratios which are 0.1, 0.3 and 0.5; the directional specimens LR and RL were tested. The applied loads were determined due to fracture toughness values. The maximum load applied should not exceed K_{max} values for proper testing. Each specimen was subjected to constant amplitude sinusoidal load. On the next step, fully reversed stress loading, which is symbolized by R= -1 is applied to both directional specimens.

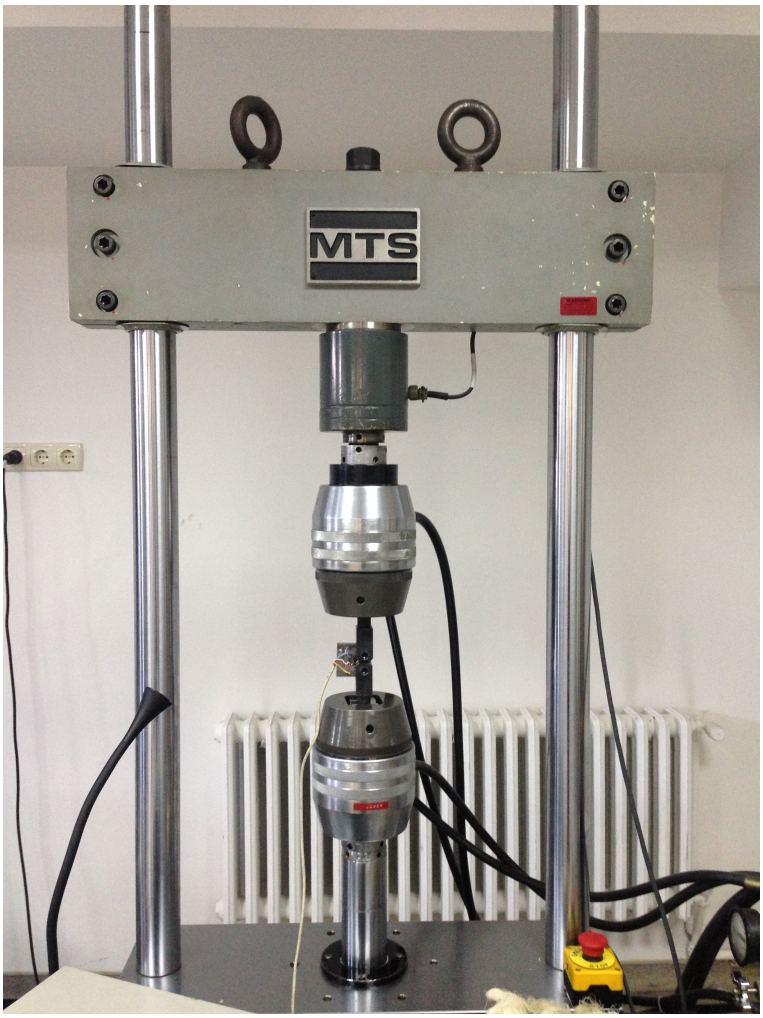

Figure 3.16. MTS 810 Universal Servo-Hydraulic Test System.

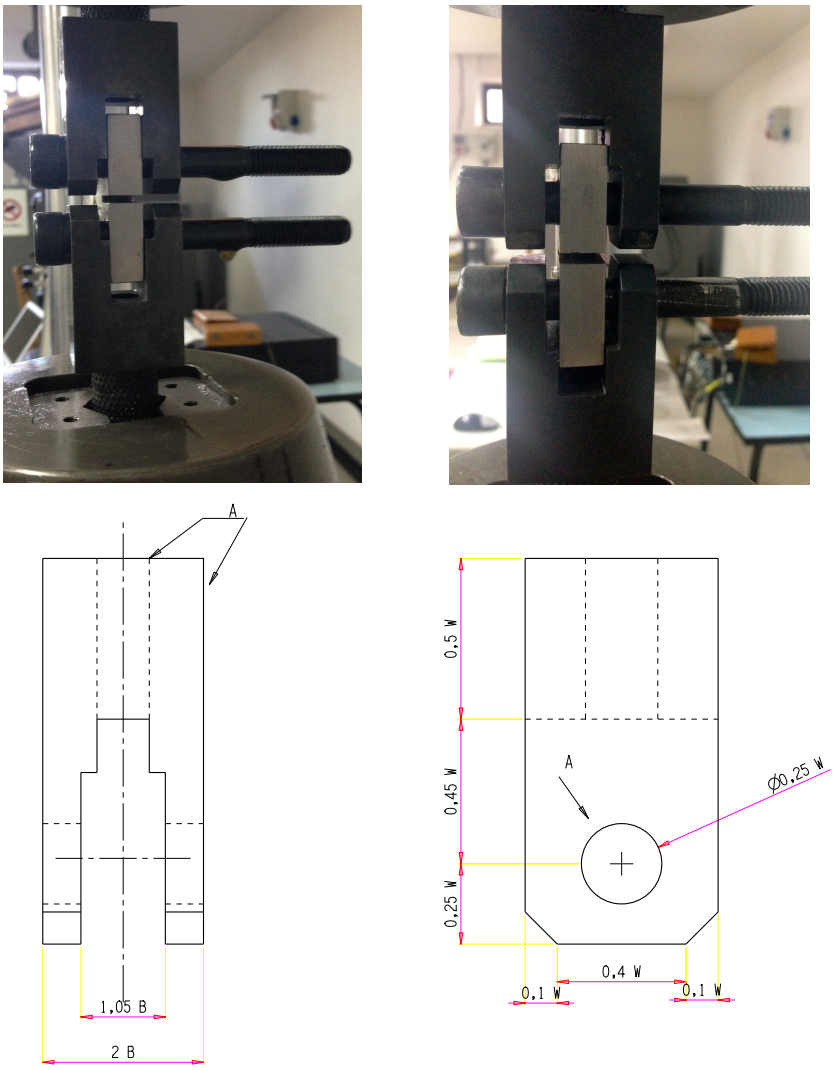

Figure 3.17. Special test apparatus used in MTS 810.

Two pairs of special apparatus was designed and machined for the tests (Figure 3.17). The first important aim of designing the apparatus was to handle the material properly in order to avoid axis shift of propagating crack. The second issue was obviously about the dimensions of the apparatus. Since the data was recorded due to electrical signals obtained from the crack gage as crack propagates, the gage should not be in contact with the apparatus.

Rumul Fractomat 7609 device is used in the analysis of fatigue crack growth behavior. One of the input channels is chosen and the connections with the specimen and MTS 810 are done properly for analysis. Consequently; the scale was fit to 0 which represents no crack growth at the beginning of each experiment.

Figure 3.18. Test equipment used for fatigue crack growth rate determination, Rumul Fractomat 7609.

The K-increasing test procedure including constant amplitude sinusoidal loading is applied during fatigue crack propagation tests. The maximum and minimum values of stresses determined due to obtained material properties such as hardness and K_{IC} fracture toughness results.

The surface finish type directly affects the life-time of the component. It is obtained that for the same specimens that only differ from each other by only the surface finish conditions; precracked, machined and polished; precracking shortens the life

time whereas polished surfaced specimens stay stable against loading up to a critical number of cycle. For the precracked specimen, crack growth begins immediately and compared to other cases, it has the shortest lifetime. The machined specimen differs slightly from the precracked one that the number of cycles are more, since the microscopic surface notches are prerequisitely required to be sharpened before crack growth. On the other hand; the polished surfaced specimen exhibits no crack growth for a long period of time, typically 30 to 80 percent of the total fatigue life. After that period, crack initiation starts and continues with crack growth. All three specimens shown on Figure 3.19 below has the same crack growth rates and the figure respresents the effects of surface finish.

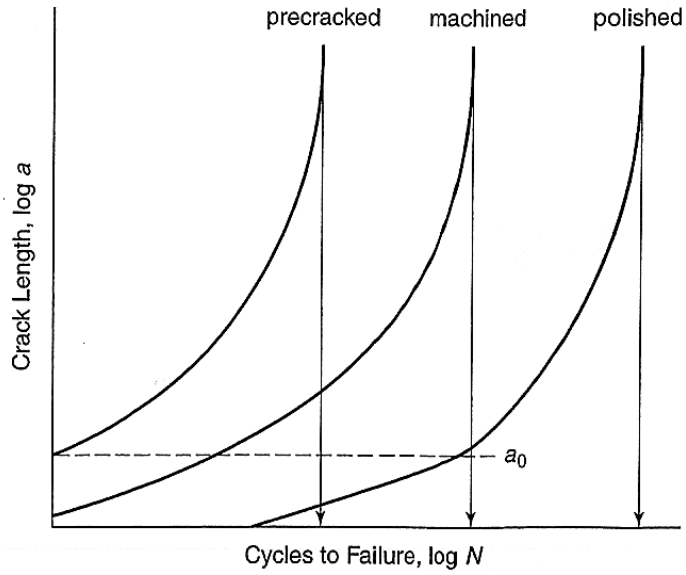

Figure 3.19. The effect of surface finish on fatigue life [34].

After precracking step due to ASTM E647 test standard, each specimen was tested to obtain crack growth rates and thus the properties of failure [5]. The minimum and maximum loads applied during tests are given on Table 3.2 below.

Table 3.2. The applied fatigue crack growth test conditions.

	R	P_{min} (N)	P_{max} (N)	f (Hz.)
RL	0.1	1200	12000	3
	0.3	3600	12000	4
	0.5	7500	15000	6
	-1	-6000	6000	5
LR	0.1	1800	18000	3
	0.3	5400	18000	3
	0.5	9000	18000	4
	-1	-7000	-7000	7

CHAPTER 4

RESULTS AND DISCUSSION

4.1. METALLOGRAPHIC EXAMINATIONS

Since the martensite structure is quite hard and brittle, it can not be used efficiently in industrial applications. In addition to this, there may exist internal stresses that causes weakness in steel. Therefore; the heat treatment, tempering, is used to eliminate these effects and relieve the internal stresses.

The appearance of modified 4340 steel in the optical microscope is dark. For deeper investigation, SEM is used. The SEM microstructural images are told to be uniform, fuzzy and dark which can be seen on Figure 4.1, 4.2 and 4.3. The structure is two-phased, consisting of α-ferrite and Fe_3C. Small cementite particles are found to be dispersed uniformly in a continuous ferrite matrix. The dark regions refer to martensite needles which transformed to α-ferrite whereas; light colored regions refer to the precipitated Fe_3C (cementite) particles during tempering [36, 47].

Due to the classification related with C wt% composition, there are two types of martensite. For 0-0.6 wt% C, martensite is called lath martensite. For compositions above 1 wt% C, the martensite is called plate martensite. Lath martensite is expected to be seen fuzzy and indistinct on images. Therefore; the image is compatible with the theoretical expectations when 0.4132 wt% C is situated.

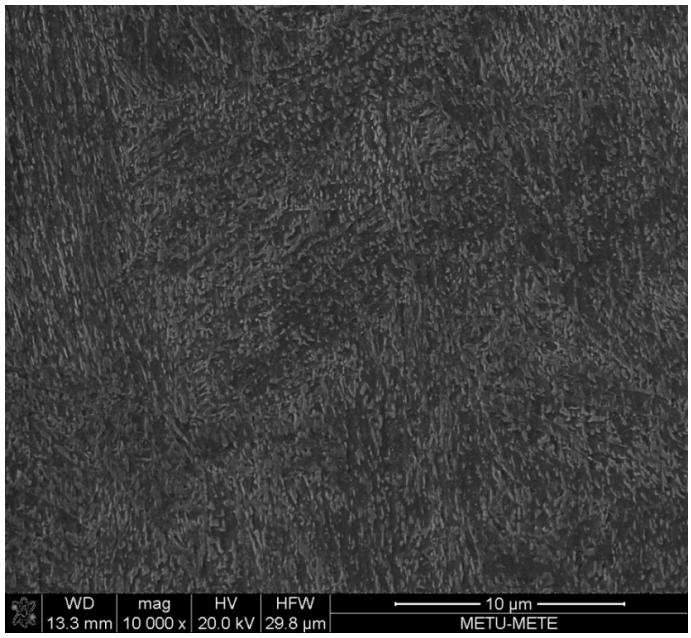

Figure 6. Microstructural image of M4340 steel under 10000x magnification.

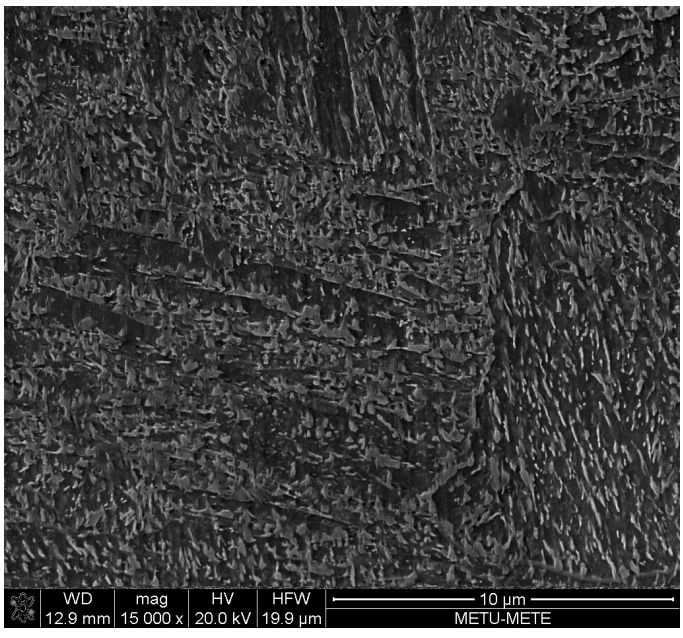

Figure 4.2. Microstructural image of M4340 steel under 15000x magnification.

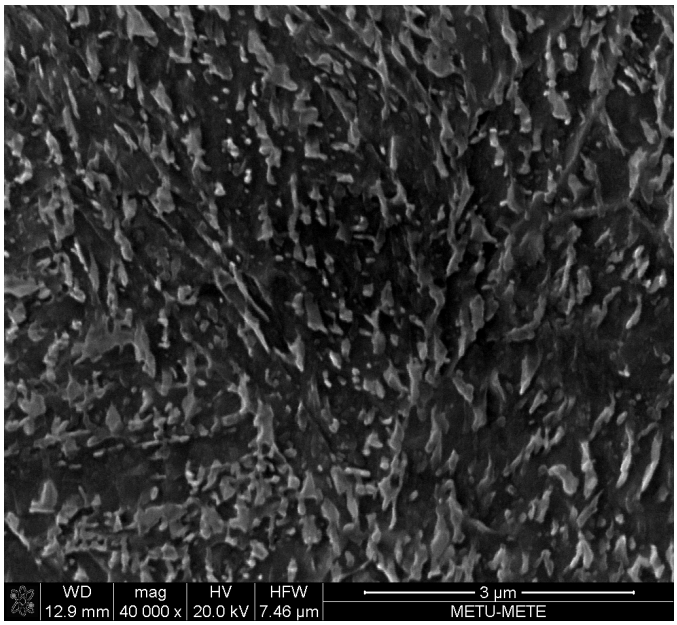

Figure 4.3. Microstructural image of M4340 steel under 40000x magnification.

4.2. SPECTRAL ANALYSIS

Compared to ASTM standard values; Mn is lower and Cr, Mo, Ni are higher in weight percent in structure. The main reasons of using low-alloy steels are to improve the hardenability of the steel and the toughness of the steel at a given level of strength.

The element sulfur is present in all steels as impurity element. There are two unique facts about sulfur impurities in iron which causes embrittlement of steel when present at low concentrations. Iron sulfide (FeS) is formed in the structure that melts at 1190 ^{o}C. Since hot rolling and forging temperatures are generally above 1190 ^{o}C, ironsulfide will be present as liquid in the structure. Secondly, the effect called *wetting* affects the structure. Small spherical balls of liquid FeS lie at the grain boundaries in steel at the hot rolling temperatures. There occurs a surface tension

force at the grain boundaries which causes the molten FeS to wet the austenite grain boundaries. The FeS is pulled into the grain boundaries as a very thin film of liquid which destroys their strength.

Manganese is mainly present in the steel structure in order to eliminate the effects of Sulfur described below. Manganese sulfide (MnS) is a compound which melts at 1655 ^{o}C -higher than FeS. In some steels, (MnFe)S is formed if the iron and manganese amounts are necessarily high and as a result. The melting temperature decreases a little but stays still high compared with the hot rolling temperatures. Therefore; the hot shortness problem is removed. Besides the removal of hot shortness problem by adding Mn the steel can lead to embrittlement problems in room temperature operations. MnS are called *inclusions* in steel and generally residual oxygen and nitrogen impurities are generated at these inclusions. The embrittlement often leads to failure but can be eliminated by other compositional changes.

The addition of Manganese and Nickel shift A1 curve down contrary to Chromium and Molybdenum as they shift it up. The addition of Manganese, Nickel, Chromium and Molybdenum does not improve the hardness of the steel much but it does increase the hardenability-the measure of the depth to which martensite can be formed.

Cr in the presence of Ni is more effective in producing finer microstructure. Chromium carbide precipitates increase the strength in such a manner that they block the grain boundaries and inhibit grain growth. The resultant structure has its grains refined and the dislocation movements get harder. Higher strength of the alloy can be achieved since chromium carbide particles in the matrix increases the energy required for elastic/plastic deformation [30].

Chromium increases the oxidation resistance of steel. is added to the steel to increase resistance to oxidation. When Cr is added to low alloy steels, an increase in the

response to heat treatment, therefore increases in hardenability and strength can be achieved.

Adding Molybdenum (Mo) into the low-alloy steel structure improves the strength and hardness at high temperature.

Besides the common usage of Nickel (Ni) in stainless steels as a corrosion resistant agent, it is used to improve oxidation and corrosion resistance. Nickel increases toughness at low temperatures when added in smaller amounts to alloy steels.

Table 4.1. Role of major alloying elements in steel alloys [31].

Element	Function
C	Solid solution strengthener, improves hardenability.
Ni	Improves toughness and hardenability, lowers transition temperature.
Cr	Improves hardenability in quenched and tempered steels, solid solution strengthener, provides corrosion resistance in stainless steels.
Mo	Improves hardenability in quenched and tempered steels, solid solution strengthener, avoids temper embrittlement.
Si	Increases yield strength and transition temperature.
Mn	Improves hardenability, deoxidizer agent, avoids wetting by forming MnS, lowerss transition temperature
Al	Forms AlN which pins grain boundaries and keeps ferrite grain size small. Improves lattice resistance to dislocation motion and lowers transition temperature.

4.3. MECHANICAL TESTS

4.3.1. TENSILE TEST

The tensile test specimens of M4340 steel machined due to TS EN ISO 6892-1 Standard were examined in the Instron 5582 tensile-compression test machine in order to determine the behavior under tensile force [26]. The Percent elongation (%) and tensile strength results obtained are shown on Table 4.2. The Tensile Stress versus Axial Strain curves of M4340 steel in longitudinal direction are given on Figure 4.5 and Figure 4.6.

The cup and cone structure has been observed after the tension tests on Figure 4.4 below. This means that the steel can promote an amount of plastic deformation before failure and as a result, ductile fracture appears.

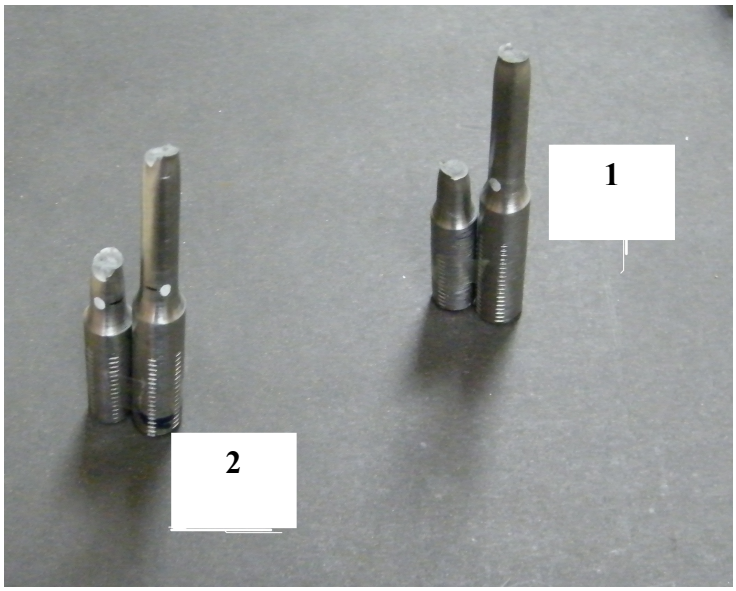

Figure 4.4. The cup and cone structure.

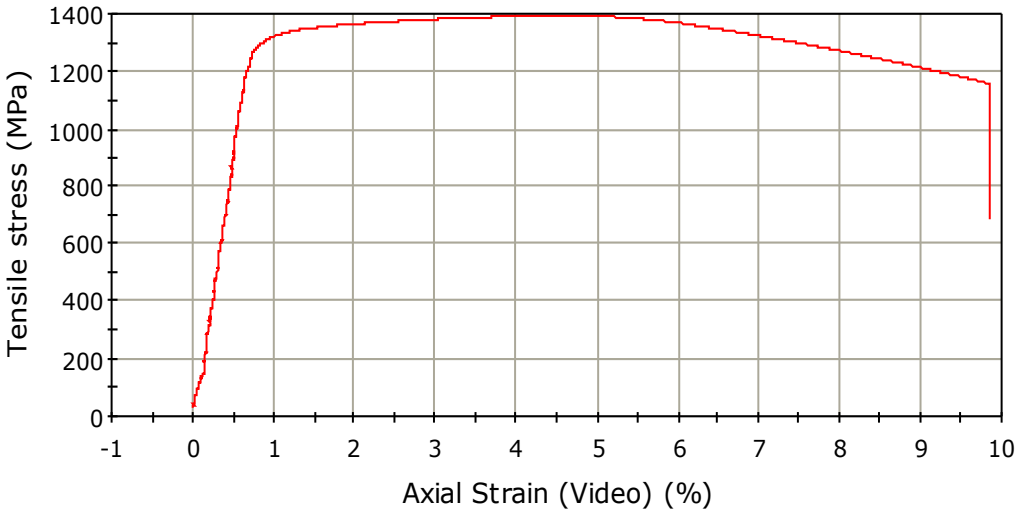

Figure 4.5. Tensile Stress vs. Axial Strain curve of longitudinal M4340 steel specimen 1.

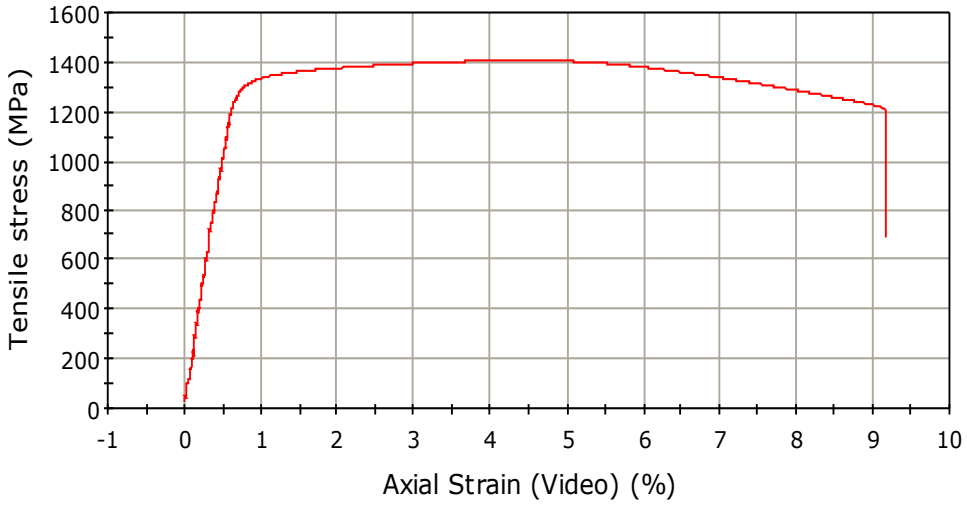

Figure 7. Tensile Stress vs. Axial Strain curve of longitudinal M4340 steel specimen 2.

Table 3.2. Tensile test results.

Specimen No.	Initial Diameter (D_0) (mm)	Initial Length (l_0) (mm)	Final Length (l_f) (mm)	Yield Strength (MPa)	Tensile Strength (MPa)	Percent Elongation (%)
Longitudinal 1	7.98	39.35	43.11	1309	1393	9.9
Longitudinal 2	7.78	38.90	42.49	1315	1407	9.2

Nascimento et al. had worked on AISI 4340 steel specimens quenched between 815-845 ^{o}C and tempered in the range of 520±5 ^{o}C for 2 h. Due to their mechanical tests conducted, the steel is found to have a 39 HRC hardness, a yield strength of 1118 MPa and an ultimate tensile strength of 1210 MPa [52]. Compared with previous study, there is an improvement of 17% and 15% on yield and ultimate strength respectively on the modified 4340 steel. This improvement can be correlated directly with the compositional changes.

4.3.2. CHARPY IMPACT TEST

Charpy Impact tests were conducted at four different temperatures which are 20 ^{o}C, 0 ^{o}C, -20 ^{o}C, -40 ^{o}C. Thermally conditioned and positioned specimens are tested. For each temperature, two specimens were tested and the absorbed energy data was recorded. On Table 4.3, the average energy values for each temperature can be seen.

Table 4.3. Charpy V-notched Impact test results of M4340 steel.

Temperature (^{o}C)	Average Energy Absorbed (J)	
	Radial 1	Radial 2
20	26.0	25.5
0	24.0	24.0
-20	24.0	20.0
-40	17.5	18.0

It is known that, for AISI 4340 steel tempered at 870 ^{o}C in the oil quenched condition, the Charpy V-notched impact energy is 10.2 Joules [35]. When compared with the results the improvement is found to be more than twice.

4.3.3. HARDNESS TEST

In order to achieve Brinell Hardness values, the measurements are conducted with 0.5 cm interval from the center of the specimen to the surface. The results are given on Table 4.4, * and ** respectively represents center and surface.

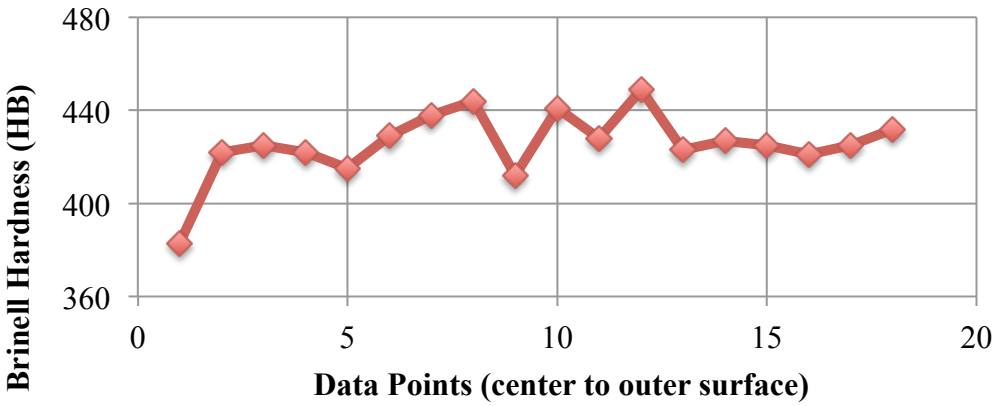

Figure 4.7. The change in Brinell Hardness from the center to surface.

Table 4.4. Brinell Hardness test results of M4340 steel specimen.

Data No.	Hardness (HB)
1*	383
2	422
3	425
4	422
5	415
6	429
7	438
8	444
9	412

Data No.	Hardness (HB)
10	441
11	428
12	449
13	423
14	427
15	425
16	421
17	425
18**	432

Since the steel billet is in cylindrical shape, the profile can be thought as the annual rings of a tree. Due to the assumption, the half profile of the billet is analyzed and assumed that the other half had the same hardness properties. On the center region,

hardness is minimum and increases till the surface. Cooling rates are always slower at the center of quenched bars. As cooling rate increases, the hardness increases [21]. With respect to changing cooling rate, hardness changes in circular manner. 39 HRC hardness obtained on Nascimento et al. studies [52], corresponds to 363 HB and it is obvious that there is an average 17% improvement on the hardness of M4340 promoted by the compositional changes .

4.3.4. PLANE-STRAIN FRACTURE TOUGHNESS TEST

Plane-strain fracture toughness tests are conducted as mentioned above on Chapter 3.4.4 above. The average of the specimen crack sizes measured from three points on the specimen are taken into consideration as the crack size (a) for each specimen. Inserting the crack size (a) and P_Q values obtained into equations 4.1 and 4.2, fracture toughness K_Q values are obtained.

$$K_Q = \frac{P_Q}{B\sqrt{W}} f\left(\frac{a}{W}\right) \tag{4.1}$$

$$f\left(\frac{a}{W}\right) = \frac{\left(2+\frac{a}{W}\right)\left[0.886+4.64\frac{a}{W}-13.32\left(\frac{a}{W}\right)^2+14.72\left(\frac{a}{W}\right)^3-5.6\left(\frac{a}{W}\right)^4\right]}{\left(1-\frac{a}{W}\right)^{3/2}} \tag{4.2}$$

Due to the restrictions on standard, the validity requirements are taken into consideration for all calculations done. The requirements can be listed as below:

1. P_{max}/P_Q should not exceed 1.1,
2. $2.5\ (K_Q/\sigma_y)^2$ must be less than the specimen ligament size (W-a).

The yield strength and plane-strain fracture toughness of AISI 4340 steel had found to be 50 MPa.$m^{1/2}$ and 87.4 MPa.$m^{1/2}$ on the previous studies [54].

Table 4.5. Yield strength and plane-strain fracture toughness of 4340 steel at room temperature.

Material	**Yield Strength (MPa)**	**Plane Strain Fracture Toughness (K_{IC}) (MPa.$m^{1/2}$)**
Alloy Steel 4340 tempered at 260 °C	1640	50.0
Alloy Steel 4340 tempered at 425 °C	1420	87.4

Table 4.6. Fracture toughness values of M4340 Steel.

	Specimen Thickness B (mm)	**Specimen Width W (mm)**	**Average Crack Size $a_{average}$ (mm)**	**Specimen Ligament Size W-a (mm)**	**P_{max} (N)**
LR1	25.09	50	26.60	23.40	35512.51
LR2	25.08	50	26.07	23.93	60496.35
LR3	25.06	50	26.04	23.96	62554.19
LR4	25.07	50	25.80	24.20	65143.47
RL1	25.03	50	26.10	23.90	47089.35
RL2	25.07	50	25.55	24.45	67263.39
RL3	25.04	50	25.69	24.31	58635.12
RL4	25.05	50	25.61	24.39	57117.81

Table 4.6 (continued). Fracture toughness values of M4340 Steel.

	P_Q (N)	Validity Requirement P_{max}/P_Q	Fracture Toughness K_Q (MPa.m$^{1/2}$)	Plane - Strain Fracture Toughness K_{IC} (MPa.m$^{1/2}$)
LR1	32709.22	1.09	60.41	60.41
LR2	54889.91	1.10	101.13	101.13
LR3	54120.97	1.16 (*)	99.59	99.59
LR4	62330.83	1.05	112.91	112.91
RL1	46969.39	1.00	86.88	86.88
RL2	67499.23	1.01	120.36	120.36
RL3	58236.98	1.01	104.89	104.89
RL4	55171.71	1.04	98.83	98.83

As the obtained fracture toughness values are compared to each other, it can be seen that both directions have nearly similar fracture toughness values but RL is slightly higher than LR which means that the M4340 steel is more resistant to crack growth on RL –having notch on longitudinal direction.

Compared to the experimental M4340 results on Table 4.6, there has been a significant improvement –on the range of 18%- on fracture toughness. This improvement is both related with compositional changes.

(*) even the first validity requirement could not been satisfied on LR3 specimen, the K_Q value is given on the related table above to give a general information.

4.3.5. FATIGUE CRACK GROWTH TEST

Fatigue crack growth tests were conducted at room temperature for different stress ratios. The applied loads are determined in such a manner that it does not exceed K_{max} and obtain observable fatigue crack growth. As previously mentioned on Chapter 3.4.5.2., the precracking step is used in order to remove the machined starter notch effects. Crack length versus Number of cycles data are obtained and with the help of a C+ programme further evaluations are done. As a result; for each distinct specimen the fatigue crack growth rates were determined. Then, the Walker equation is applied to each of the curves.

On Figure 4.8.a-4.8.h crack length vs. number of cycle curves are given below. For each directional specimen RL and LR, the crack length versus number of cycles for failure curves are compared for each stress ratios respectively. Afterwards; the fatigue crack growth rate vs. ΔK graphs are given between Figure 4.11.a and Figure 4.11-h.

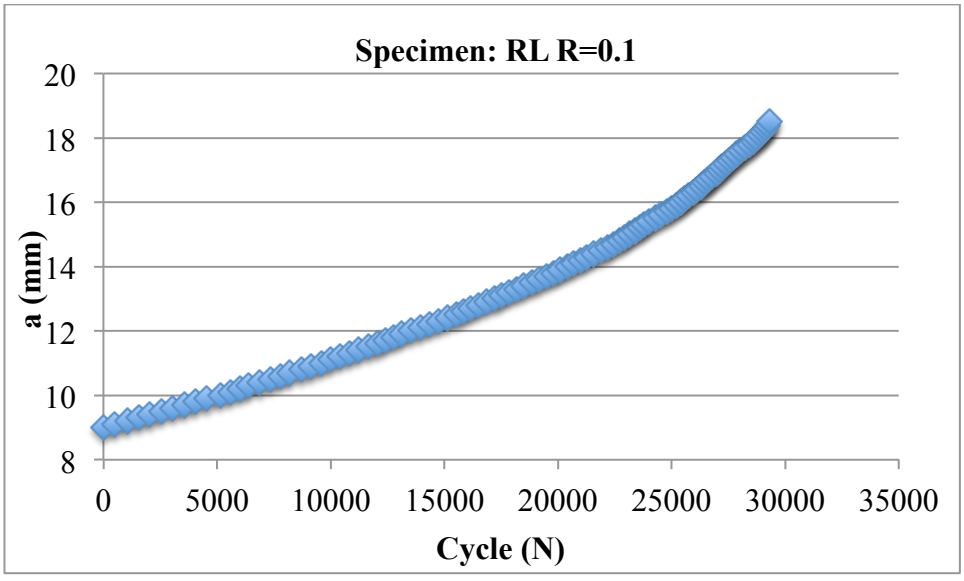

Figure 4.8.a. Crack length vs. number of cycles of M4340-RL specimen for R=0.1.

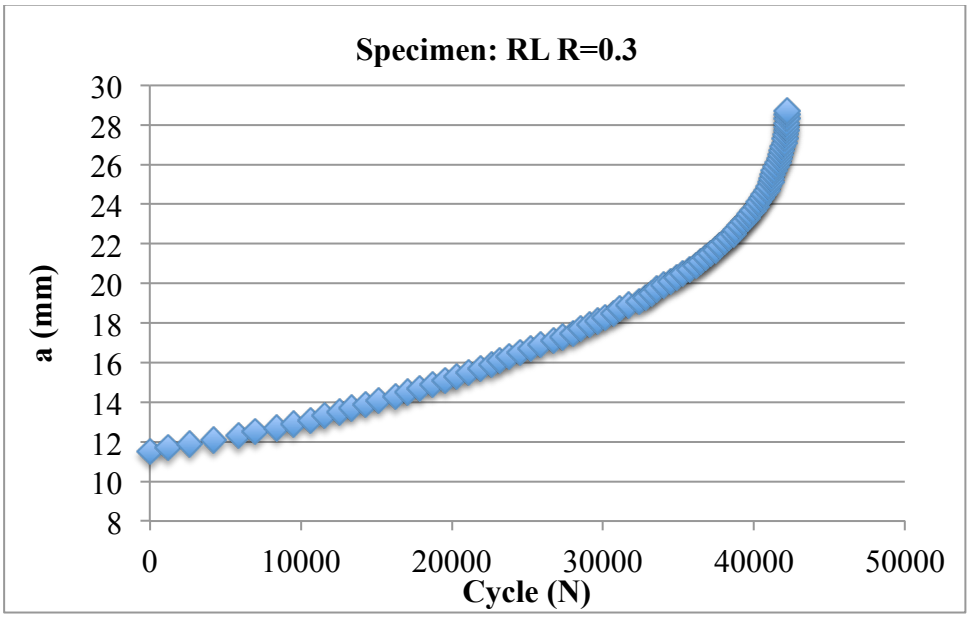

Figure 4.8.b. Crack length vs. number of cycles of M4340-RL specimen for R=0.3.

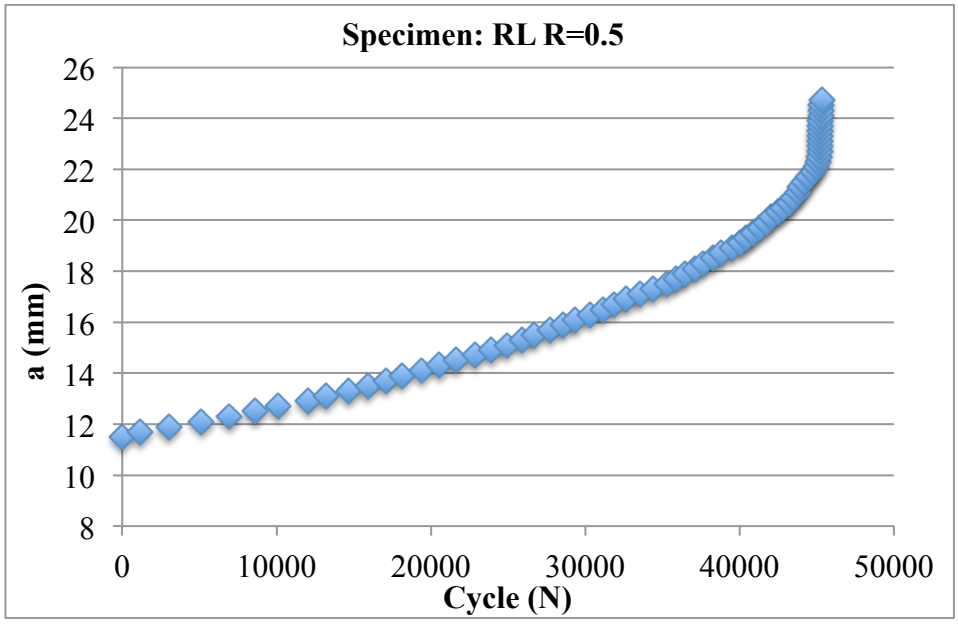

Figure 4.8.c. Crack length vs. number of cycles of M4340-RL specimen for R=0.5.

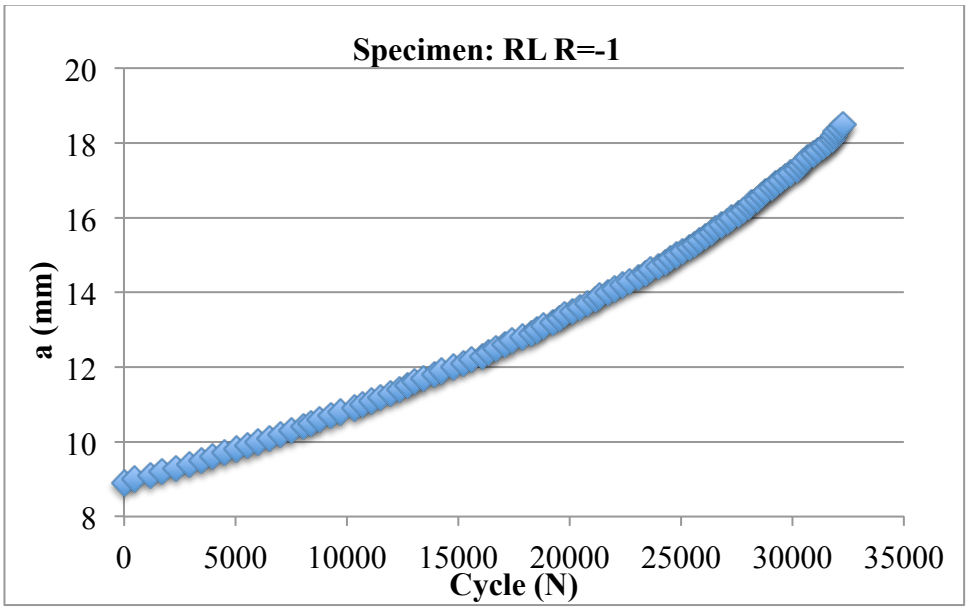

Figure 4.8.d. Crack length vs. number of cycles of M4340-RL specimen for R=-1.

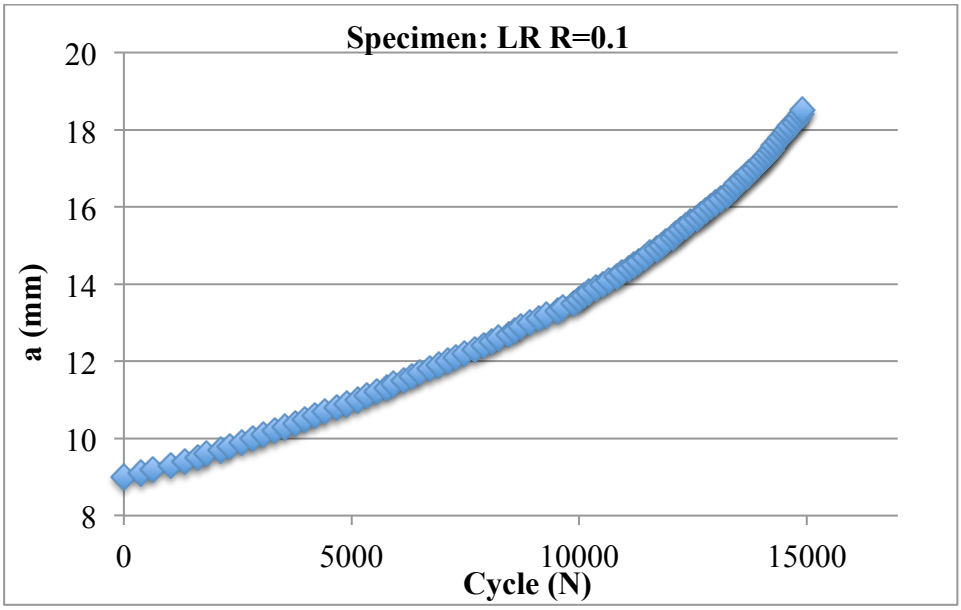

Figure 4.8.e. Crack length vs. number of cycles of M4340-LR specimen for R=0.1.

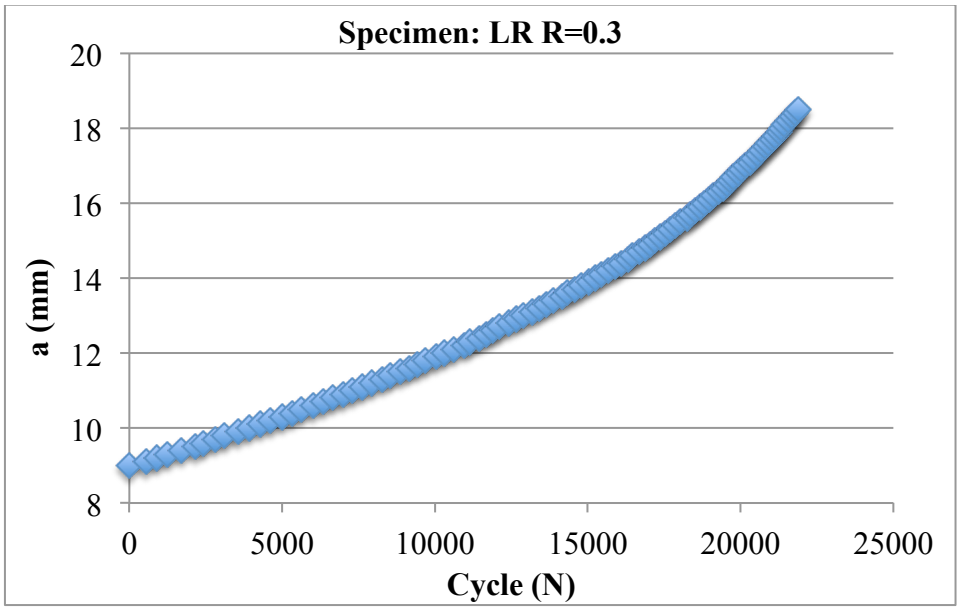

Figure 4.8.f. Crack length vs. number of cycles of M4340-LR specimen for R=0.3.

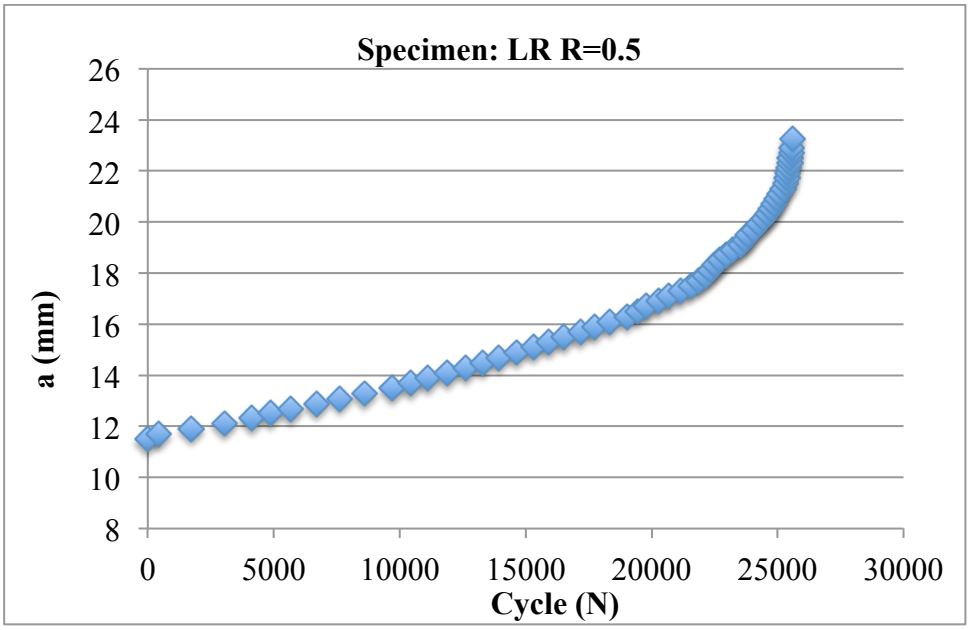

Figure 4.8.g. Crack length vs. number of cycles of M4340-LR specimen for R=0.5.

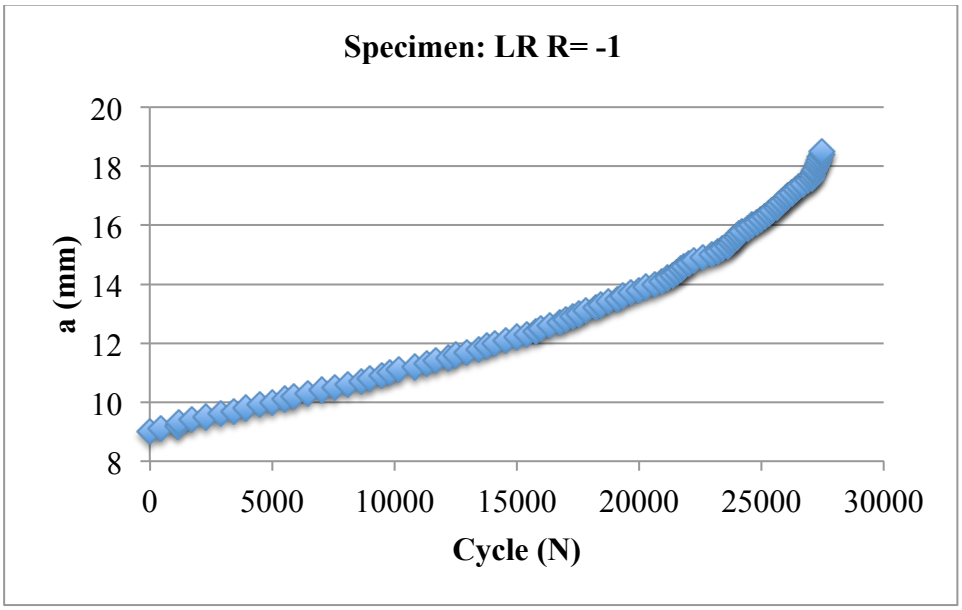

Figure 4.8.h. Crack length vs. number of cycles of M4340-LR specimen for R=-1.

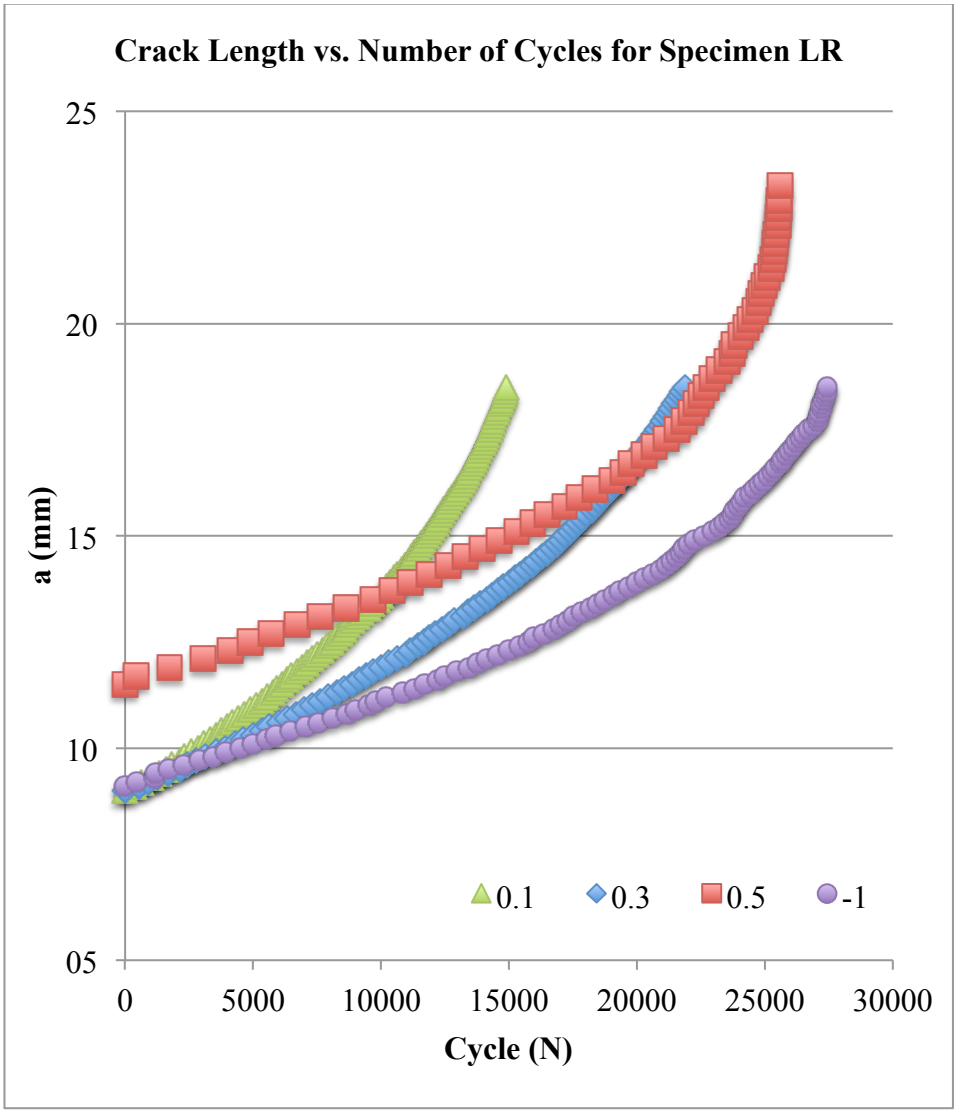

Figure 4.9. Crack length vs. number of cycles of M4340-LR specimens.

For LR and RL directional specimens, all a-N curves belonging to changing stress ratios are placed on the same graph and given on Figure 4.9 and 4.10 respectively.

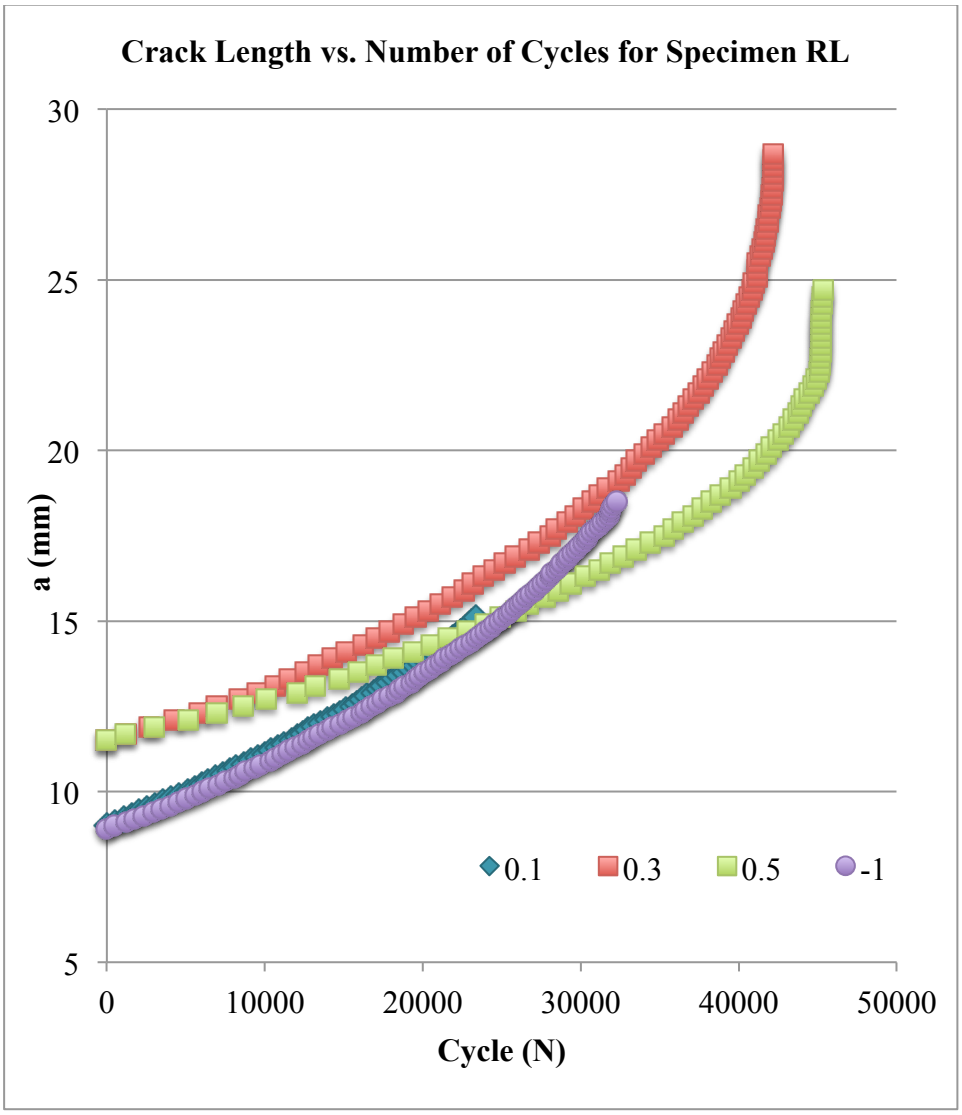

Figure 4.10. Crack length vs. number of cycles of M4340-RL specimens.

It is mathematically evident that the quadratic 7-point incremental polynomial method introduces quite a smoothing effect in reducing the amount of data scatter and thus the data variance. Therefore; incremental polynomial method was chosen and applied for best fitting curve and fatigue behavior evaluation [5]. The obtained result curves of crack growth rate vs. ΔK are given from figure 4.11.a to 4.11.h.

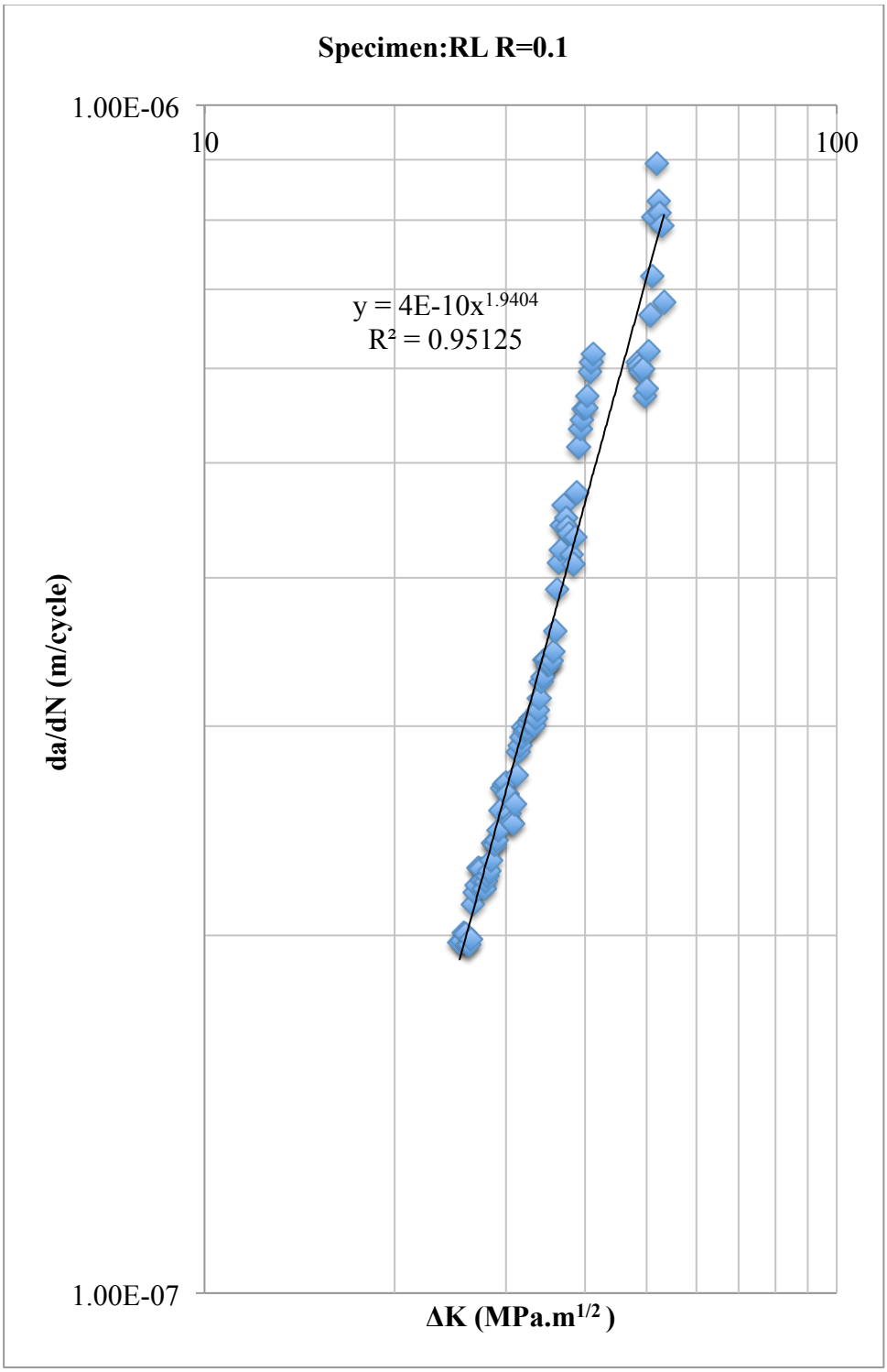

Figure 4.11.a. Crack growth rate versus stress intensity curve for M4340-RL specimen for R=0.1.

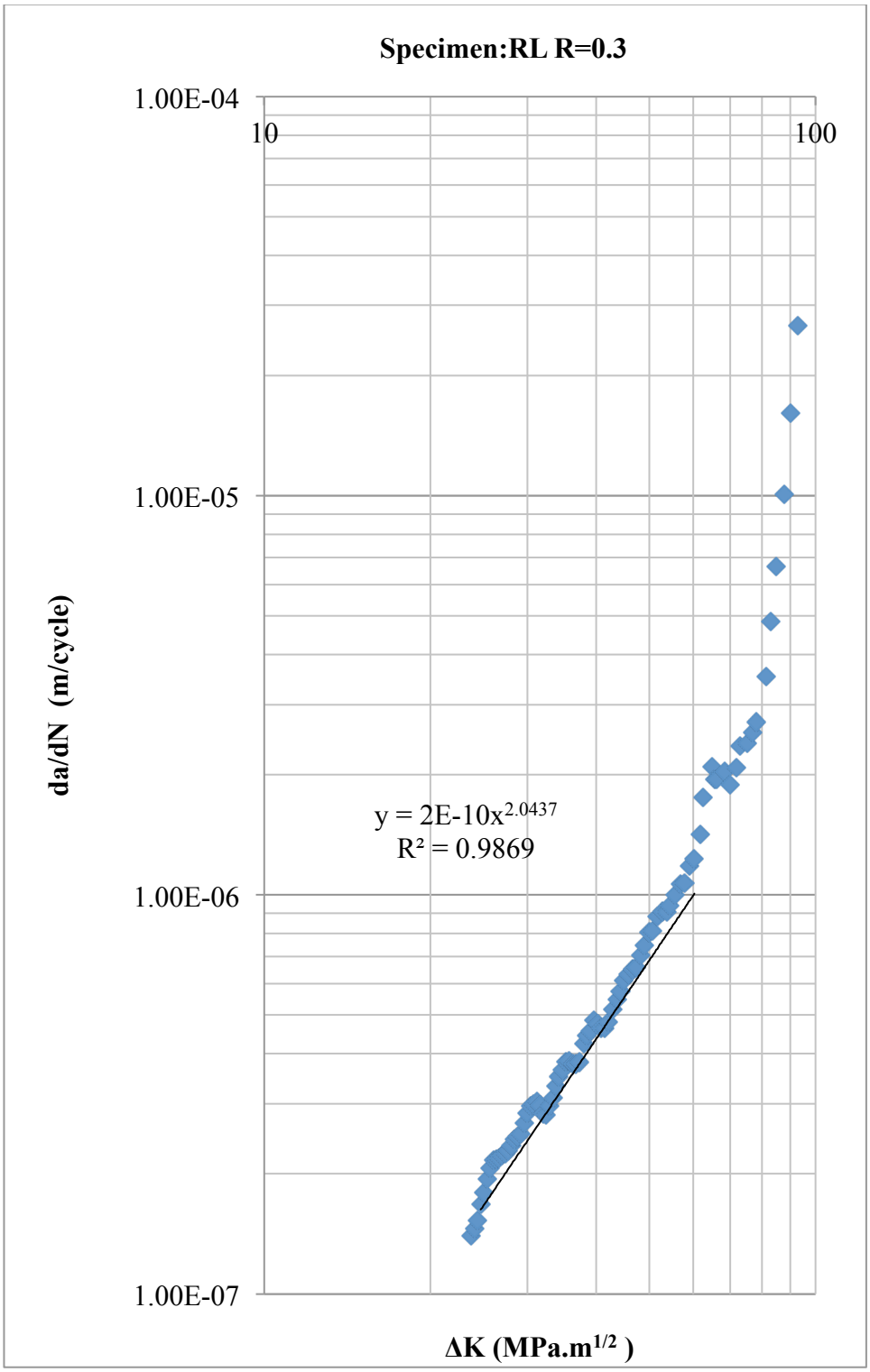

Figure 4.11.b. Crack growth rate versus stress intensity curve for M4340-RL specimen for R=0.3.

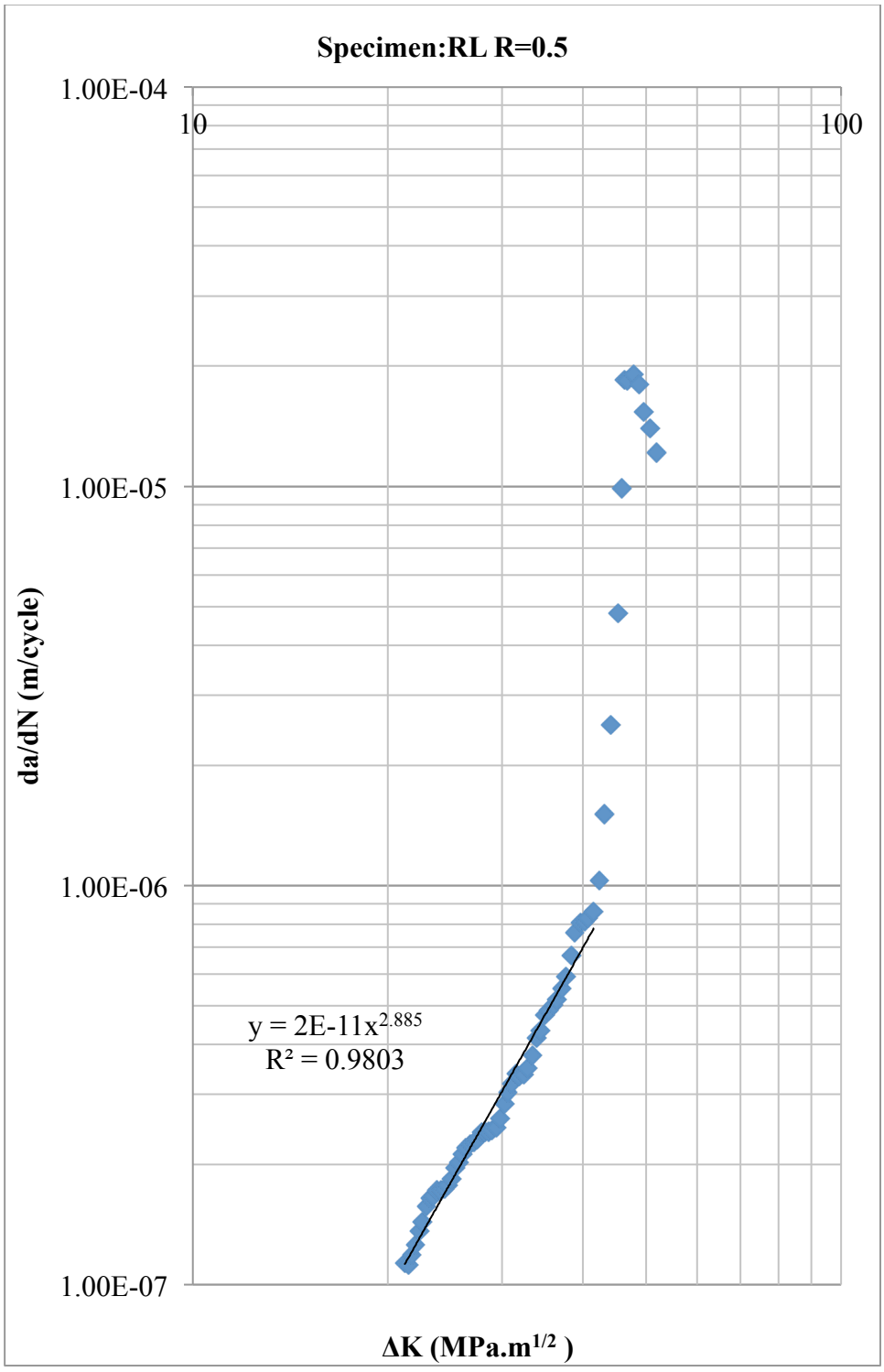

Figure 4.11.c. Crack growth rate versus stress intensity curve for M4340-RL specimen for R=0.5.

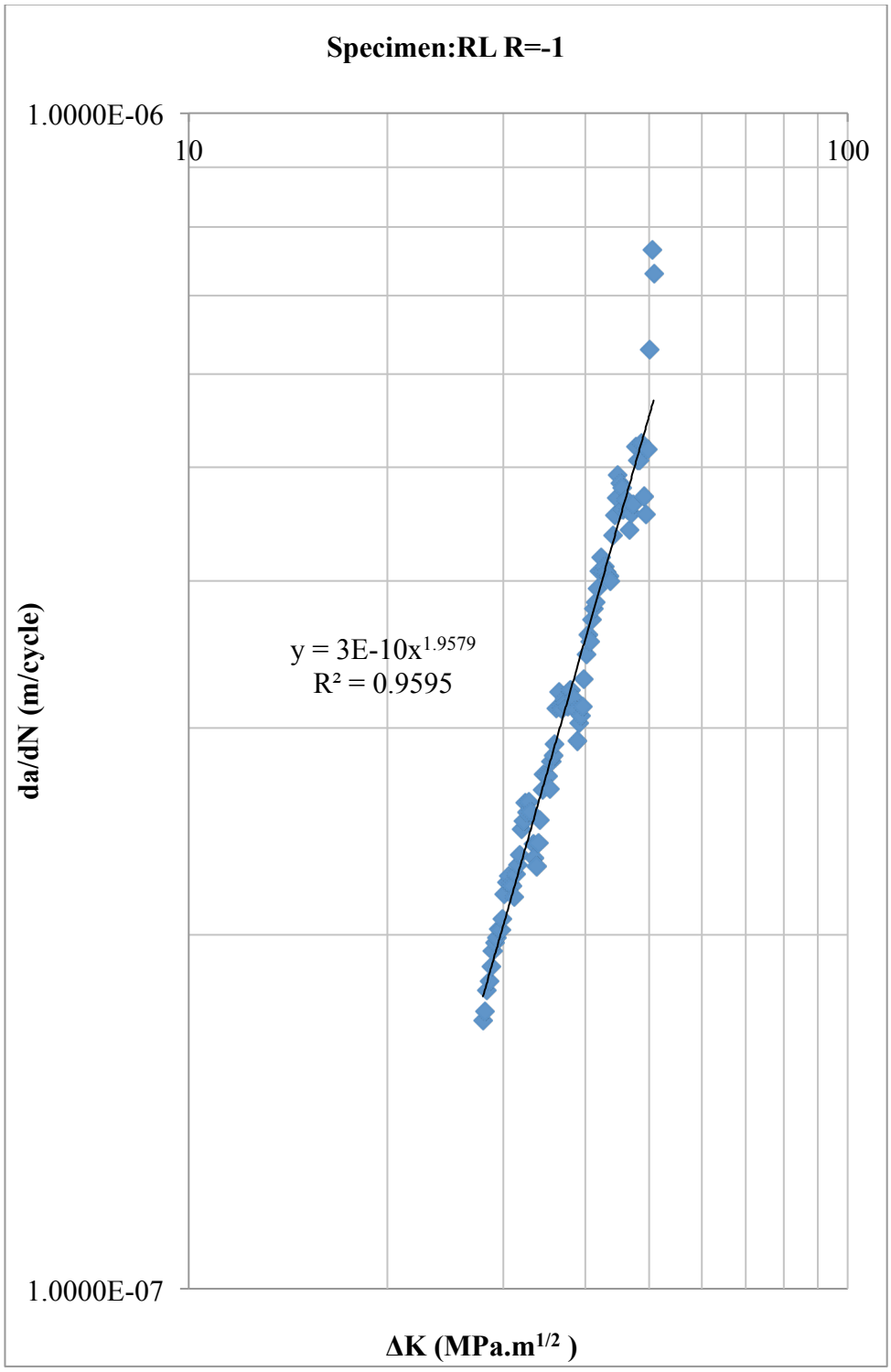

Figure 4.11.d. Crack growth rate versus stress intensity curve for M4340-RL specimen for R= -1.

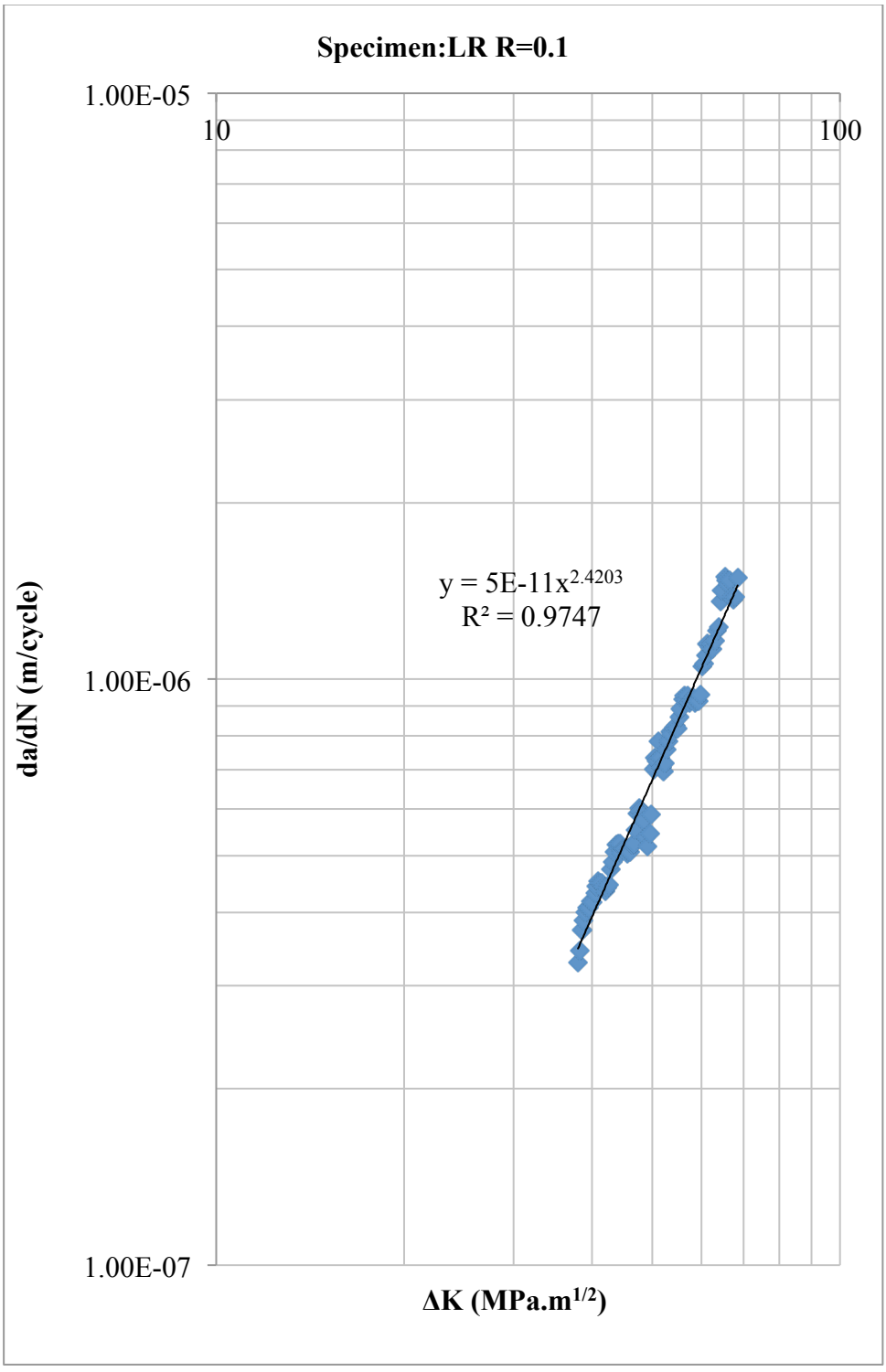

Figure 4.11.e. Crack growth rate versus stress intensity curve for M4340-LR specimen for R=0.1.

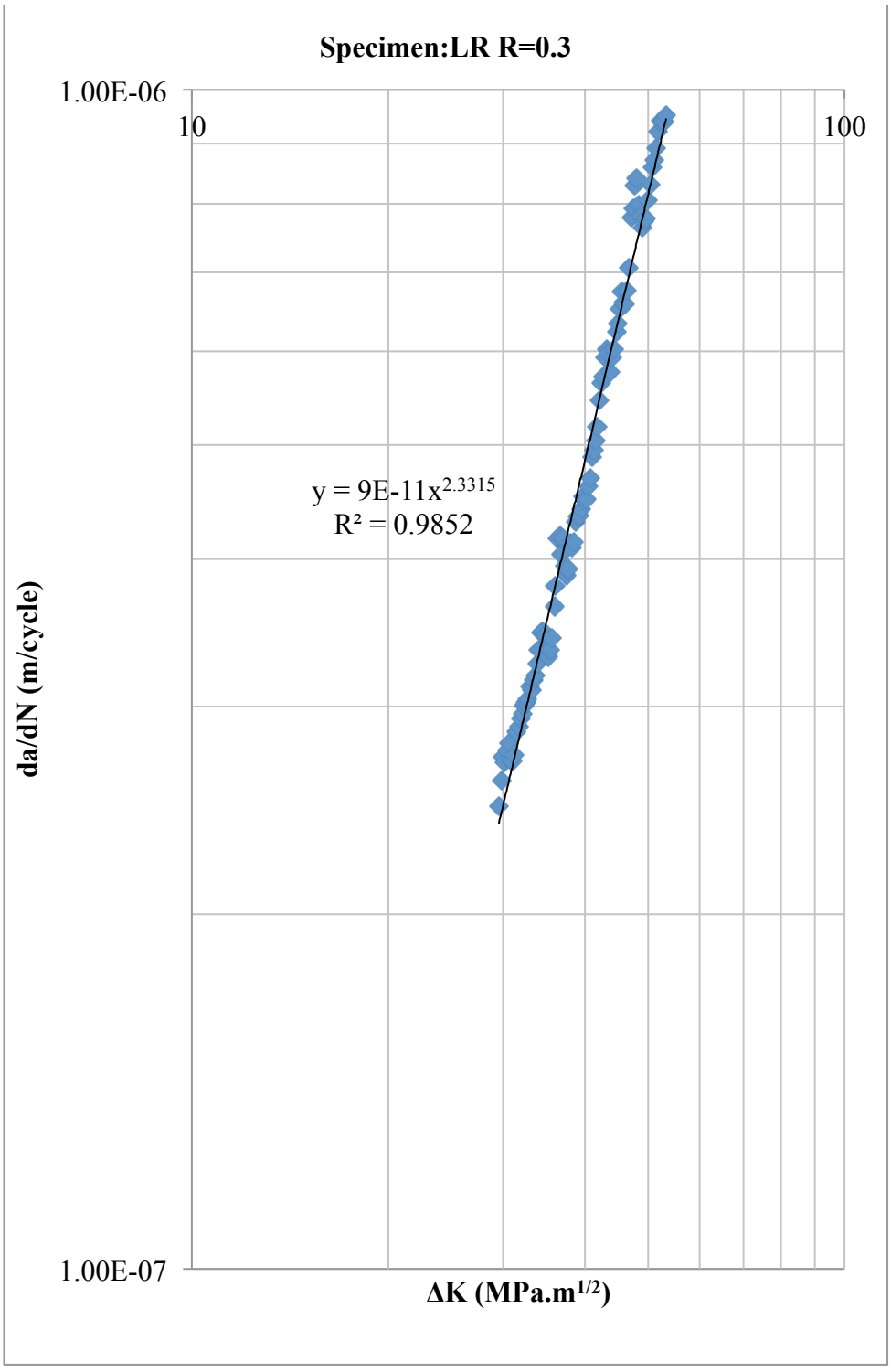

Figure 4.11.f. Crack growth rate versus stress intensity curve for M4340-LR specimen for R=0.3.

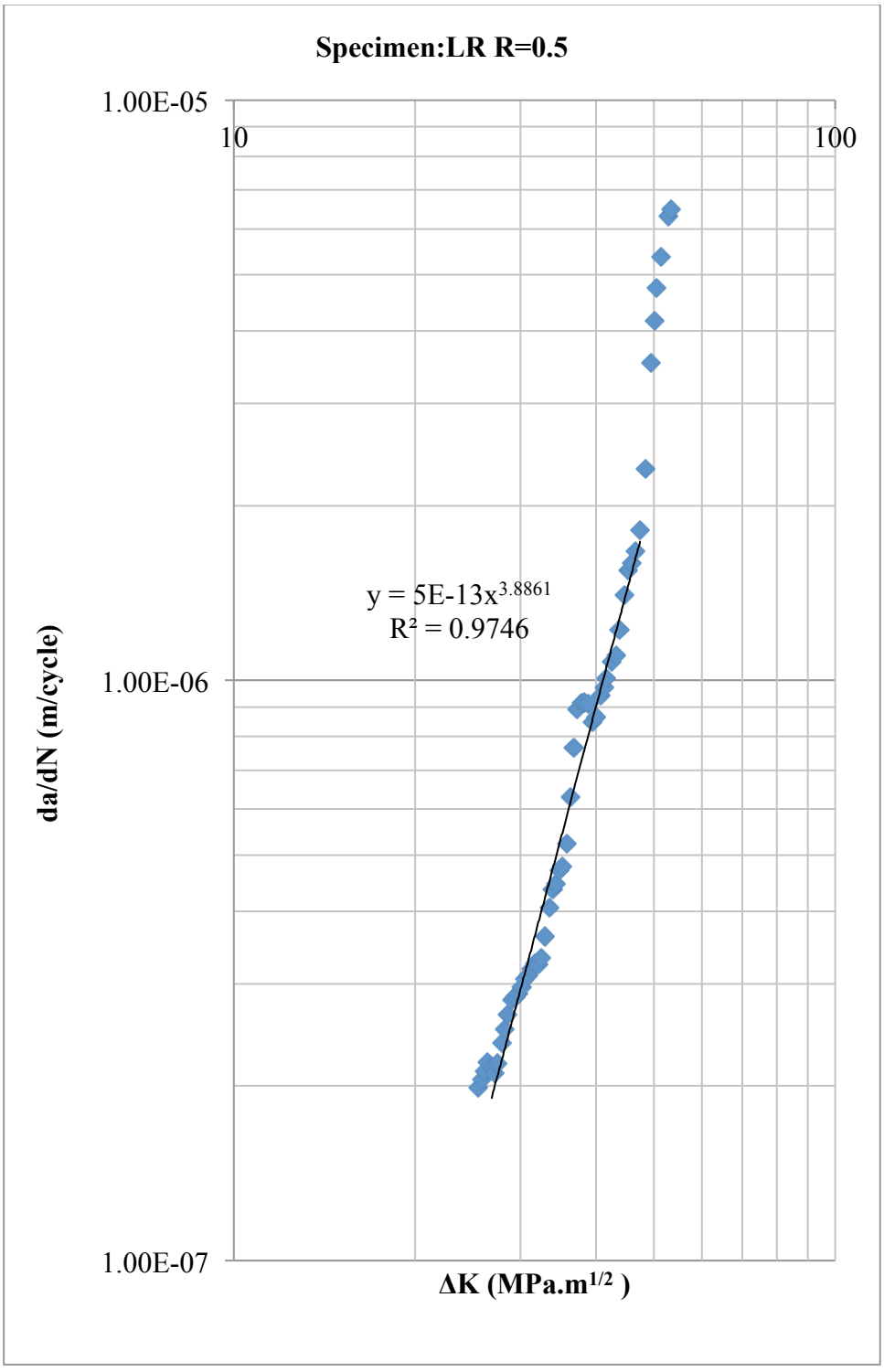

Figure 4.11.g. Crack growth rate versus stress intensity curve for M4340-LR specimen for R=0.5.

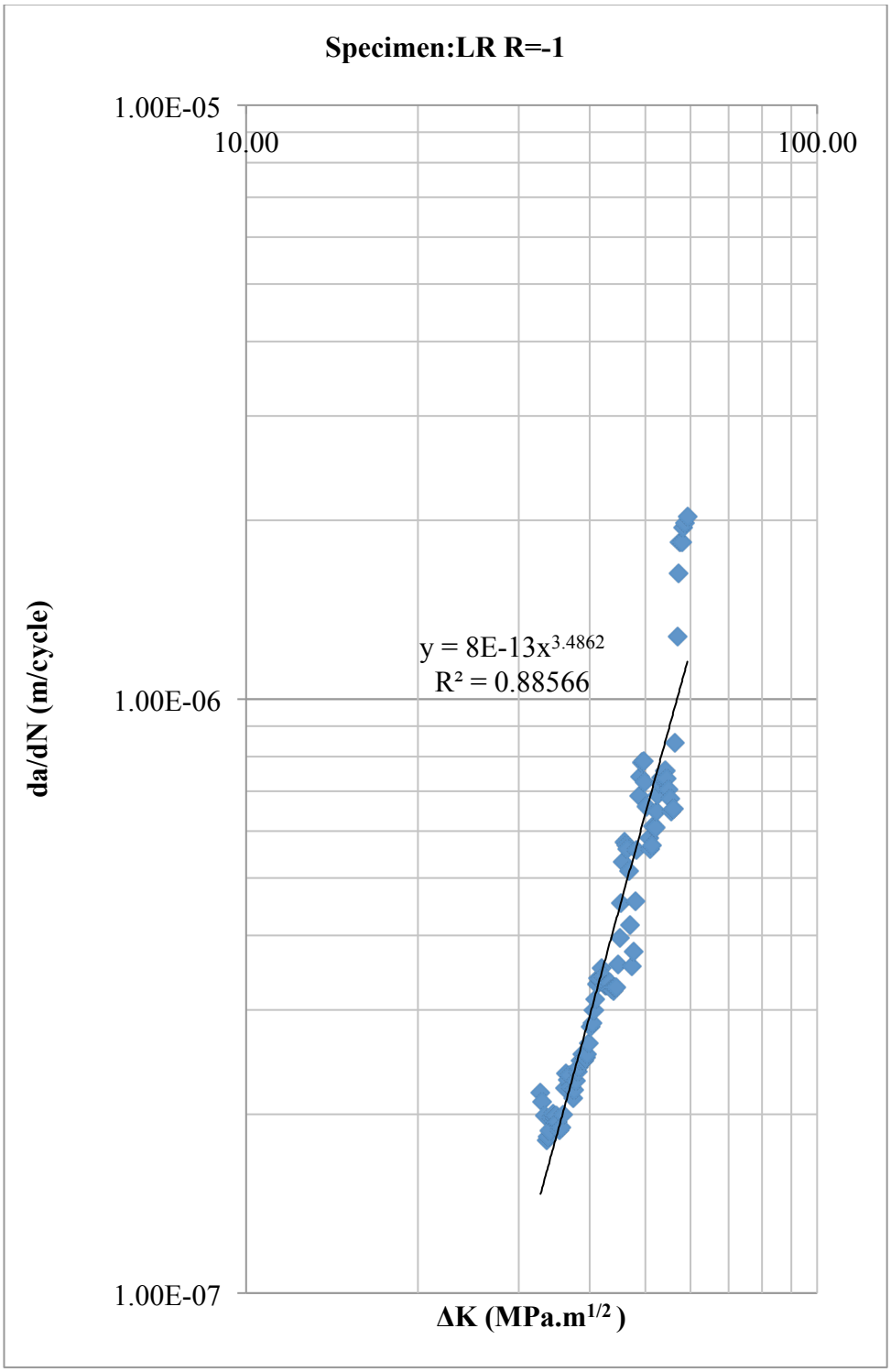

Figure 4.11.h. Crack growth rate versus stress intensity curve for M4340-LR specimen for R=-1.

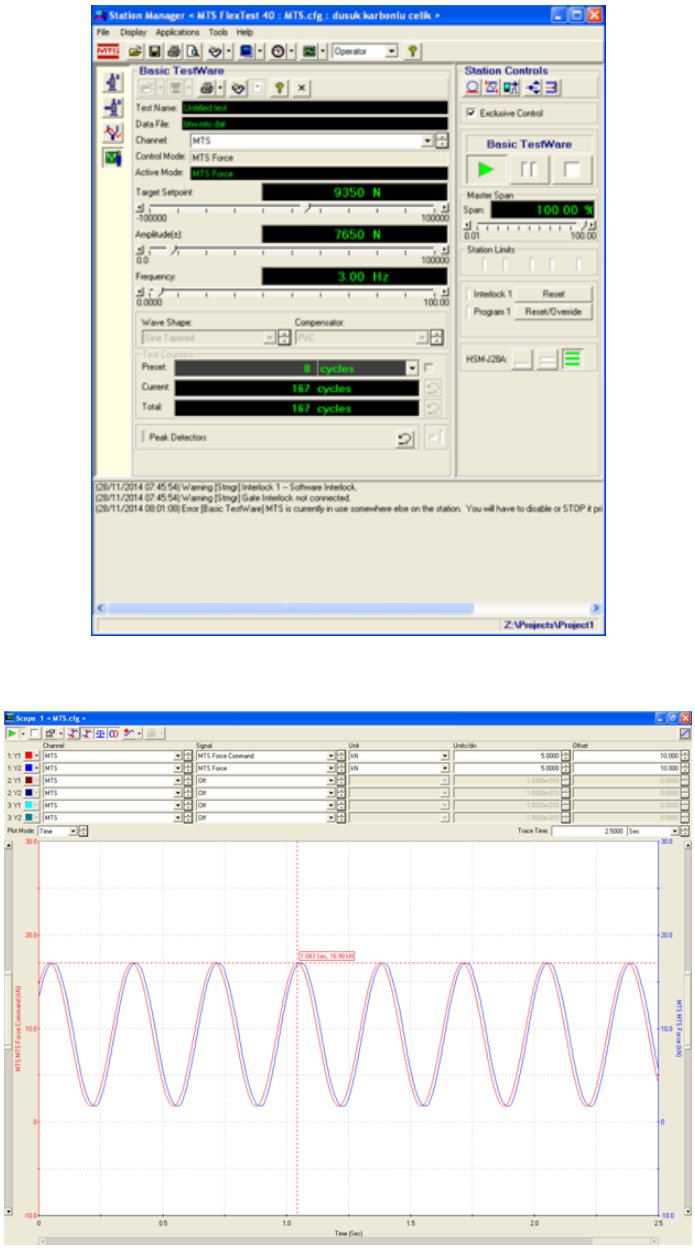

Figure 4.12. The screenshots of the control panel of MTS.

On Figure 43, a sample control panel screenshot is shown. The amplitude, frequency and target set point values define directly the sinusoidal curve applied to the specimen for fatigue crack growth rate tests itself.

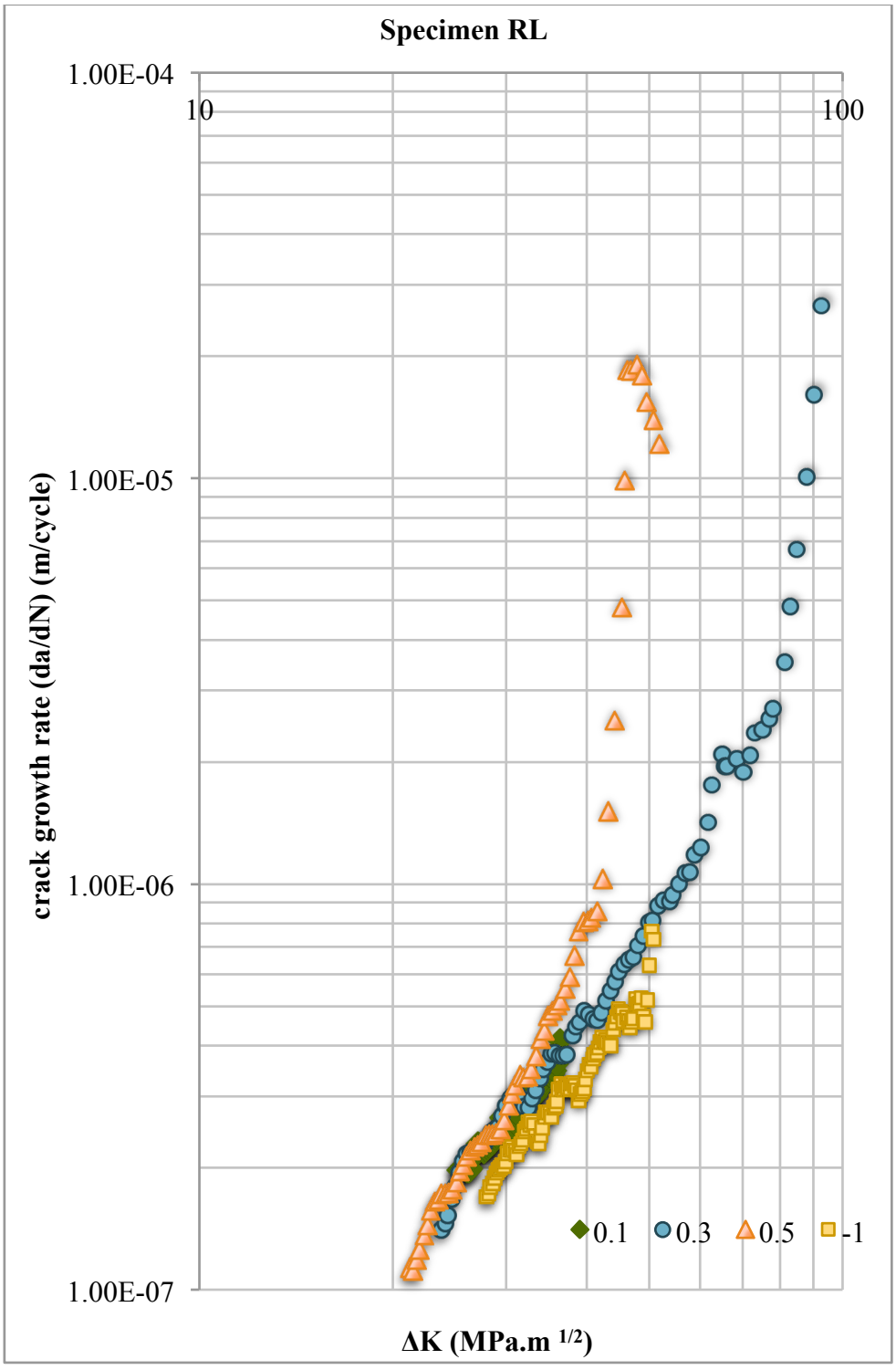

Figure 4.13. Changing R ratio effects on da/dN vs. ΔK curves for specimen RL.

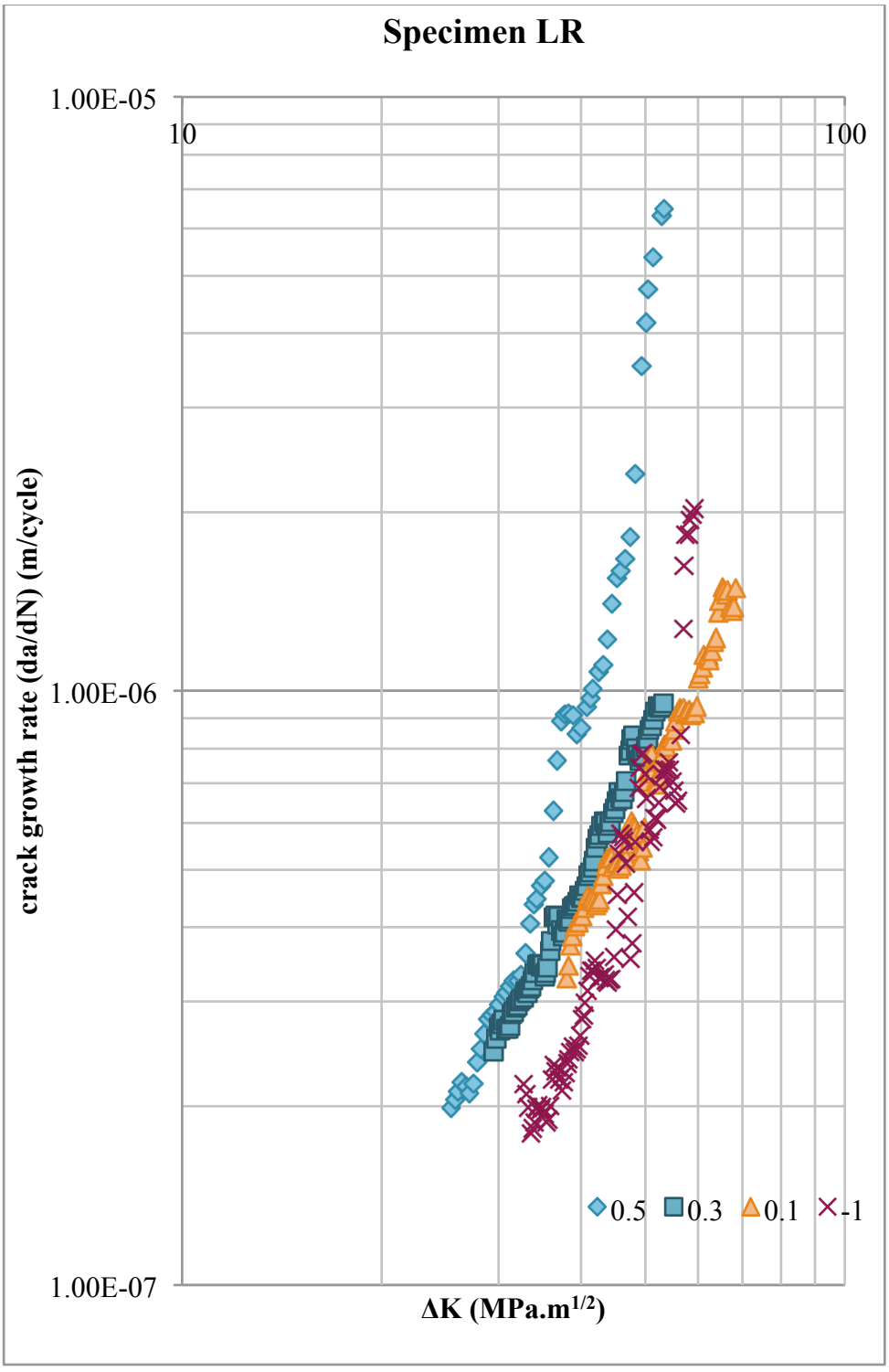

Figure 4.14. Changing R ratio effects on da/dN vs. ΔK curves for specimen LR.

Paris-Erdogan Law is used in data evaluation for all data including reverse stress cycle loading condition. First of all; the constant amplitude loading test data, the crack length versus number of cycle, is reduced by using seven-point incremental method and crack growth rates are obtained. The linear part of each fatigue crack growth data are fitted to a best line and the line determining constants C, n and R^2 are obtained from MS Excel (Table 4.7).

Table 4.7. Paris-Erdogan Law equation constants for each specimen.

	R	**C**	**n**	**R^2**
RL	**0.1**	4.0E-10	1.9404	0.9513
	0.3	2.0E-10	2.0437	0.9869
	0.5	2.0E-11	2.8850	0.9803
	-1	3.0E-10	1.9579	0.9595
LR	**0.1**	5.0E-11	2.4203	0.9747
	0.3	9.0E-11	2.3315	0.9852
	0.5	5.0E-13	3.8861	0.9746
	-1	8.0E-13	3.4862	0.8857

Moreover, besides Paris-Erdogan law, Walker Equation is used in the evaluation of fatigue data. Since the Walker Equation is only applicable to positive stress ratio conditions, except R= -1 conditions, all data sets are analyzed as mentioned below and the Walker Equation constants are obtained.

Using MS Excel; $y = A * x^B$ power type fit is applied to each data set and the constants are determined for each graph as given on Table 11 below where;

$$\mathrm{A} = \frac{\mathrm{C}}{((1-\mathrm{R})^{(1-\mathrm{m})})^{\mathrm{n}}} \text{ and } B = n.$$

The equivalent stress intensity factor ($\Delta \mathrm{K_{eq}}$) term is taken into consideration for the best fit between the test data and predicted values.

$$\frac{\mathrm{da}}{\mathrm{dN}} = \mathrm{C}(\Delta \mathrm{K_{eq.}})^{\mathrm{n}}$$

$$\Delta \mathrm{K_{eq.}} = \frac{\Delta \mathrm{K}}{(1-\mathrm{R})^{(1-\mathrm{m})}}$$

Since the ΔK_{eq} versus da/dN curves on log-log plot should fall on the same line for the same specimen, which is independent of changing stress ratio, the experimental data are tried to fit on the same line by changing constant m for all data belonging to specimen RL and LR. For best fit; m is selected for each directional specimen by trial-error method. Due to the best m value which superposes all lines, other constants n and C are calculated as given on Table 4.8.

Table 4.8. Walker equation constants for each specimen.

	R	A	B	m
RL	**0.1**	4.0E-10	1.940	0.90
	0.3	2.0E-10	2.044	0.90
	0.5	2.0E-11	2.885	0.90
LR	**0.1**	5.0E-11	2.420	0.59
	0.3	9.0E-11	2.332	0.59
	0.5	5.0E-13	3.886	0.59

	R	n	C	R^2
RL	**0.1**	1.940	3.88E-10	0.9613
	0.3	2.044	1.86E-10	0.9911
	0.5	2.885	1.64E-11	0.9850
LR	**0.1**	2.420	4.50E-11	0.9821
	0.3	2.332	6.40E-11	0.9901
	0.5	3.886	1.66E-13	0.9777

On the next step, each data set is processed in MATLAB. By using "*Curve Fitting Tool",* the parameters calculated due to Walker equation are defined as a result, the best line and R^2 values has obtained.

Finally; R^2 values on Table 4.7 and 4.8 are compared. As a result; Walker equation is found to fit the experimental data better than Paris-Erdogan since it contains the effect of stress ratio. It can easily be said that Walker Equation is an improved model compared to the precursor model Paris-Erdogan.

4.3.6. FRACTOGRAPHY

The fracture surfaces of RL and LR directional specimens were examined on the last step of the experimental study. The scanning electron microscope is used during examinations. SEM micrographs of specimen LR were given on Figure 4.15, 4.16 and 4.17. On the first photomicrograph; the fatigue region and unstable fast crack growth region can be seen clearly with the border distinguishing both under x100 magnification. The upper smooth area indicates the stable crack growth including beach marks. When the crack exceeds the fatigue threshold of region II, the crack propagation becomes irregular and the crack growth rate increases leading to failure. Therefore; final fracture region presents a fibrous and irregular aspect.

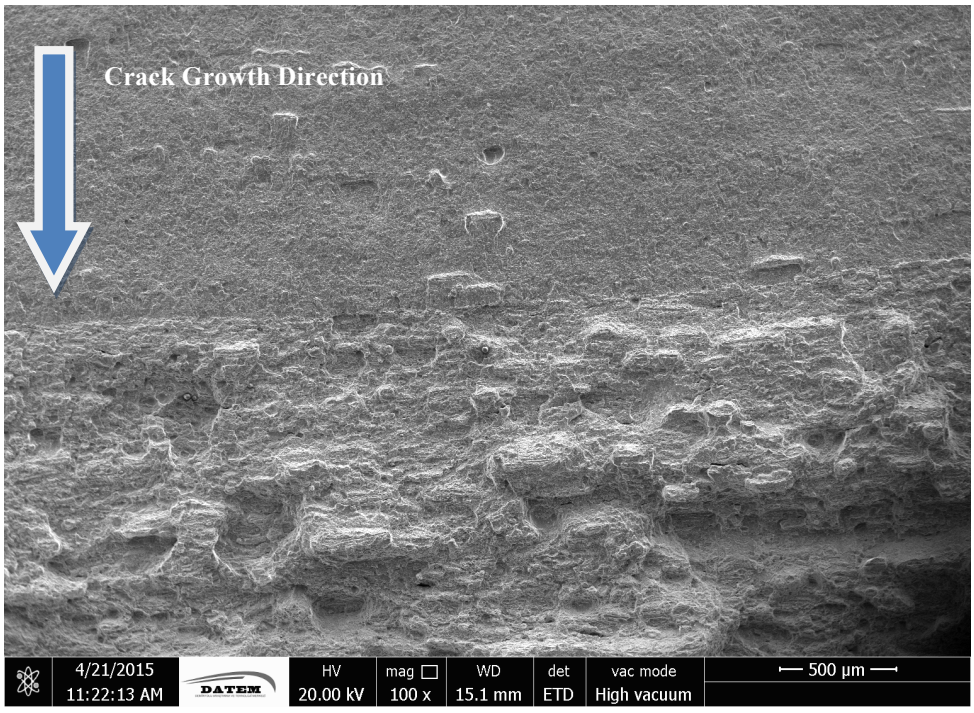

Figure 4.15. Fracture surface of specimen LR.

On Figure 4.16 below, the striations belonging to the stable crack growth region of specimen LR is clearly seen under 5000 magnification. The crack propagation region can be described by beach marks and striations. Since the striations are microscopic features and beach marks are macroscopic; striations can only be seen on suitable magnifications. Each striation corresponds to a load cycle and it is sensible to mention that when striations are present, there is fatigue on the material.

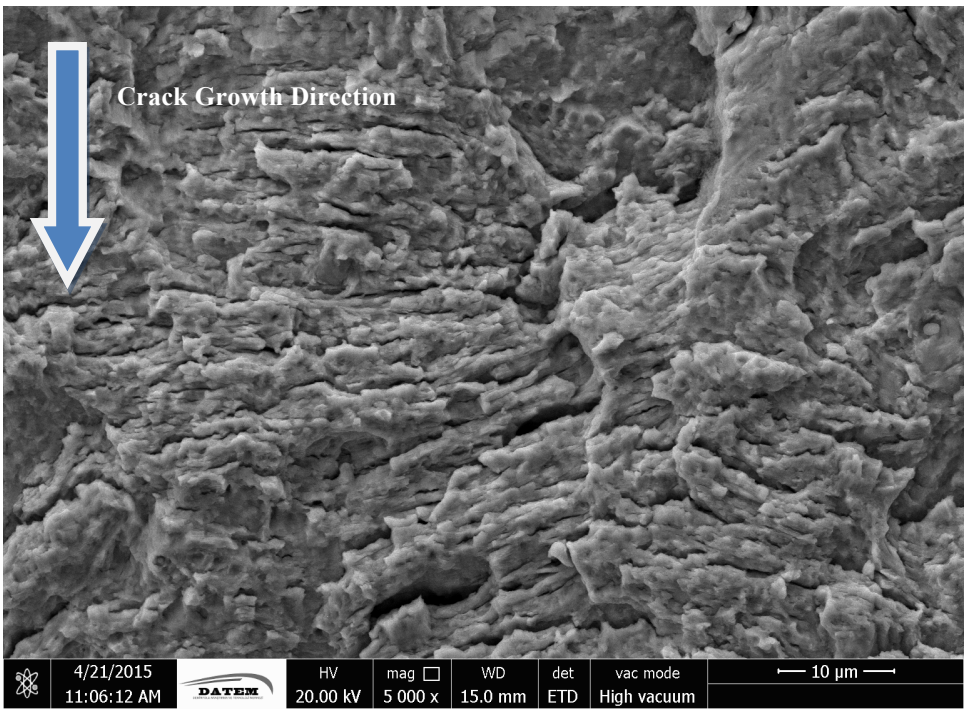

Figure 4.16. Micrograph showing striations on specimen LR.

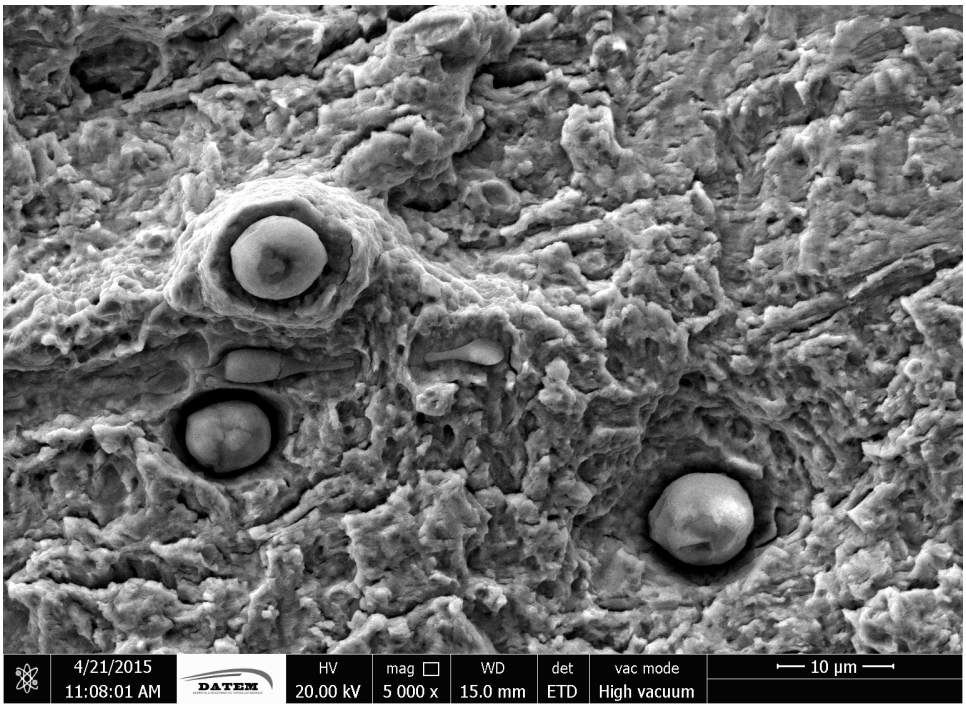

Figure 4.17. Inclusions present on Specimen LR.

Some inclusions were seen in the structure during SEM examination (Figure 4.17). These structures are thought to block and slow the rate of crack growth. In order to understand the structure and the composition of it, the left upper structure's composition had been analyzed by EDS, additionally (Figure 4.18). The EDS spectrum is given on Figure 4.19. Due to spectrum analysis, 20.53% of Oxygen and 19.06% of Silicon were present in weight percentages.

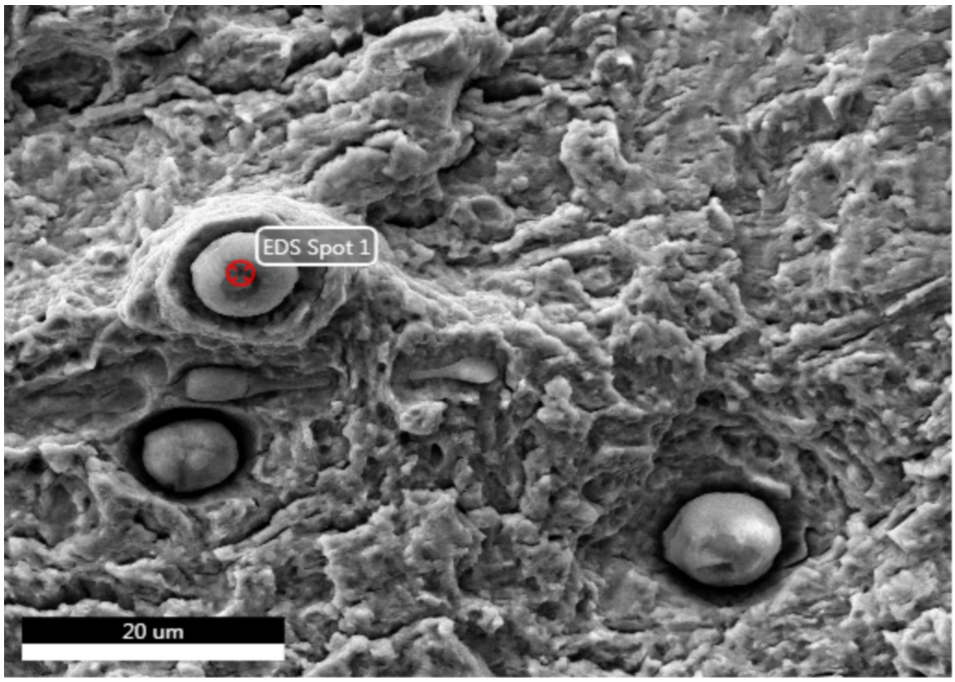

Figure 4.18. The selected area for EDS analysis.

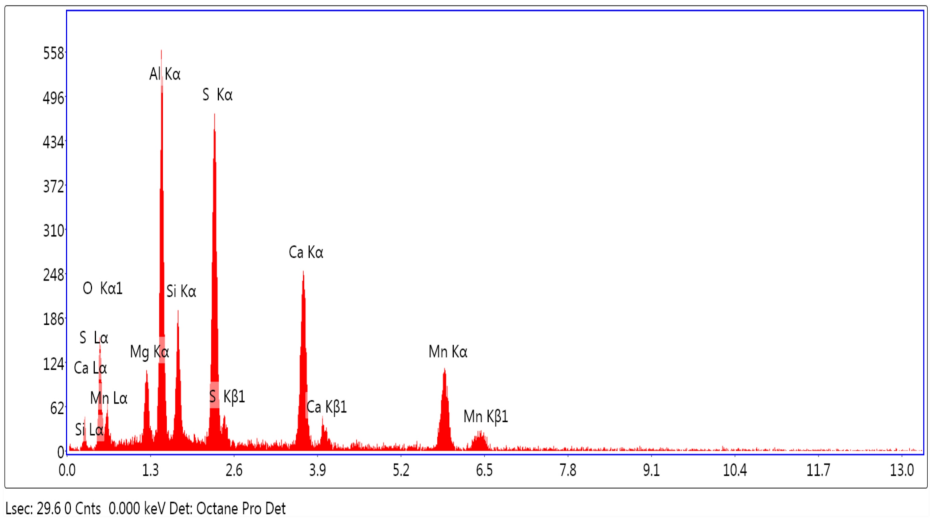

Figure 4.19. EDS Spectrum of spot-1 point.

Table 4.9. Compositional distribution of the selected inclusion-1.

Element	wt%
O	20.53
Mg	4.16
Al	17.60
Si	6.45
S	19.06
Ca	16.25
Mn	15.95

Furthermore; Figure 4.20 shows striations of specimen RL which has the perpendicular direction of crack growth compared to Specimen LR under x24000 magnification.

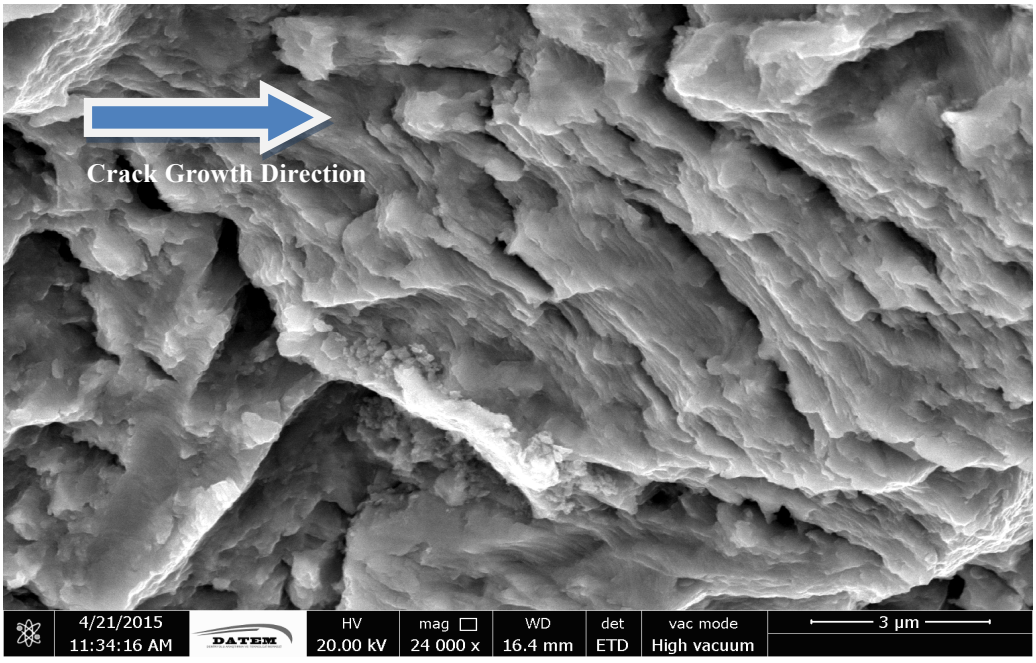

Figure 4.20. Striations of Specimen RL.

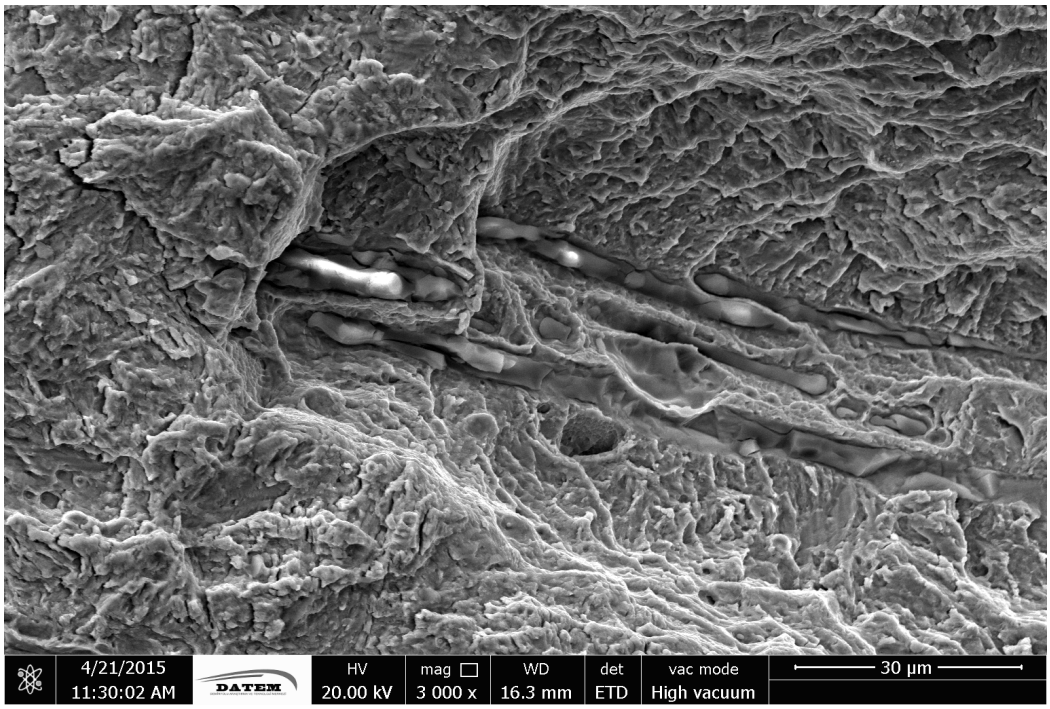

Figure 4.21. Inclusions on steel structure under 3000x magnification.

Even though the steel structure had been refined by several advanced techniques mentioned above such as electroslag refining and vacuum degassing, there can be residual inclusions which can not be eliminated completely. On Figure 4.21; some residual inclusions are given. The EDS analysis results are given on Table 4.10.

Table 4.10. Compositional distribution of the selected inclusion on RL.

Element	weight%	atomic%
OK	38.49	56.19
MgK	0.70	0.68
AlK	17.98	15.56
SiK	14.10	11.71
SK	0.37	0.27
CaK	22.62	13.18
FeK	5.74	2.40

The microtopograph below is characterized by numerous dimples from microvoid coalescence (Figure 4.22). The dimples are subcomponents of microvoids which develop very near the advancing crack front as the metal is being strained. The dimpled structure obtained from the final fracture region shows that the fracture is of ductile fracture.

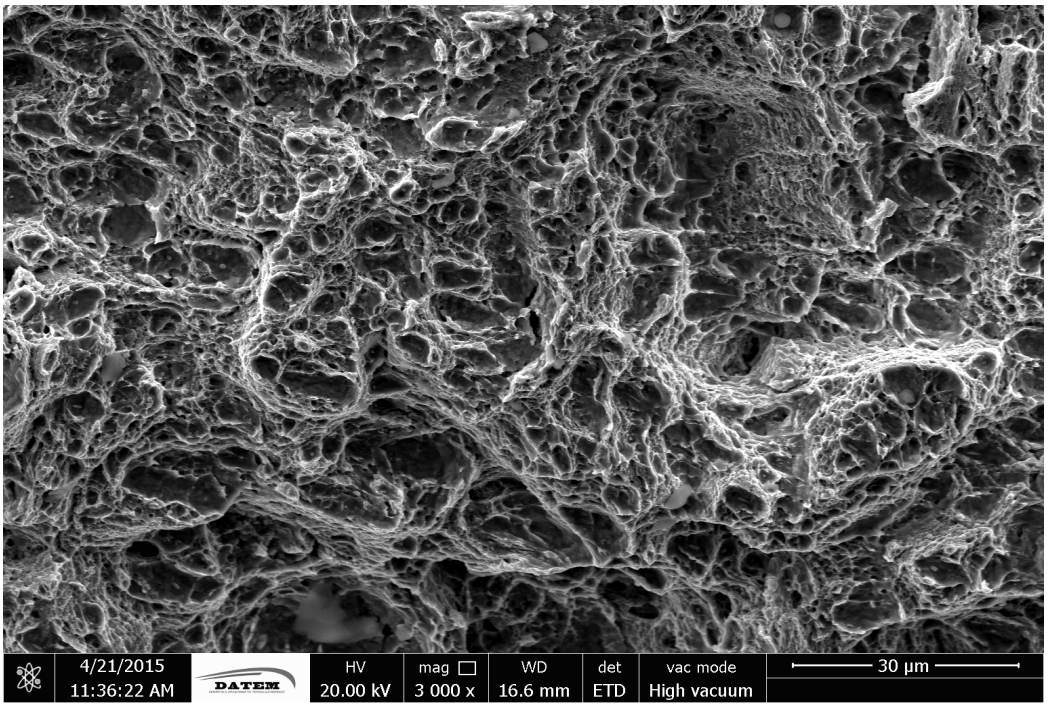

Figure 4.22. Fractograph showing dimples of Specimen RL.

CHAPTER 5

CONCLUSION

- A minimum improvement of 15% elongation has been detected due to compositional changes. The unique constant for each material which is plane-strain fracture toughness is found to be improved from 80 MPa.$m^{1/2}$ to 100-105 MPa.$m^{1/2}$ which corresponds to an increase of 25%. All these upgrades can be related with ESR and vacuum degassing besides compositional modifications.

- The two directional specimens RL and LR are analyzed in terms of their strength and it is seen that the steel is more resistant in direction RL which has the higher K_{IC} and has expected crack growth on longitudinal plane. At constant ΔK, crack growth rate increases with increasing stress ratio from -1 to 0.5. The crack growth rate of RL is lower compared to LR. The crack growth rate comparison compromises the K_{IC} comparison. The higher the $K_{IC,}$ the slower the crack growth rate.

- For the same crack length (a), number of cycles required increases with increasing positive stress ratio (R) values from 0.1 to 0.5.

- Fatigue crack growth rate increases as stress ratio (R) increases in positive. As stress ratio increases, ΔK_{th} shifts to left-lower values. Mean stress directly affects the fatigue behavior in such a manner that; as mean stress increases, lifetime decreases.

- Walker Equation fits the experimental data better than Paris-Erdogan as expected since it contains the stress ratio effects in itself.

- The fractographs show that the fracture is in ductile manner including dimples.

- When the compositional changes are assessed, it is seen that the addition of Molybdenum, Chromium and Nickel improves strength of the steel structure compared to standard AISI 4340 steel.

REFERENCES

1. C. Bathias, A. Pineau, “Fatigue Of Materials And Structures-Fundamentals”, John Wiley&Sons Inc., pp. 1-5, 2010.

2. J. E. Bringas, ASTM Handbook Of Comparative World Steel Standards, 2nd edition, ASTM DS67A.

3. W. A. Wood, “Some Basic Studies Of Fatigue Metals In Fracture”, John Wiley & Sons Inc., NY, 1959.

4. C. Laird, “Fatigue Crack Propagation”, ASTM Spec. Tech. Publ., 415, pp. 131-168, 1967.

5. ASTM E647-08, “Standard Test Method For Measurement Of Fatigue Crack Growth Rates”, ASTM International, 2008.

6. B. Mukherjee, “A Note On The Analysis Of Fatigue Crack Growth Data”, International Journal of Fracture, 8, pp. 449- 451, 1972.

7. R. A. Smith, “The Determination Of Fatigue Crack Growth Rates From Experimental Data”, International Journal of Fracture, 9, pp. 352-355, 1973.

8. K.B. Davies, C.E. Feddersen, “Evaluation Of Fatigue-Crack Growth Rates By Polynomial Curve Fitting”, International Journal of Fracture, 9, pp. 116-118, 1973.

9. H. G. Munro, “The Determination Of Fatigue Crack Growth Rates By Data Smoothing Technique”, International Journal of Fracture, 9, pp. 366-368, 1973.

10. J. Polak, Z. Knesl, “On The Fatigue Crack Growth Rate Evaluation From Experimental Data”, International Journal of Fracture, 11, pp. 693-696, 1975.

11. J. R. Mohanty, B. B. Verma. P. K. Ray, “Determination Of Fatigue Crack Growth Rate From Experimental Data: A New Approach”, Int. J. Microstructure and Materials Properties, 5, No. 1, pp. 79-87, 2010.

12. S. J. Hudak, R. J. Bucci (editors), “Fatigue Crack Growth Measurement and Data Analysis: A Symposium”, 738, pp. 93-97, 1981.

13. Ralph I. Stephens, Ali Fatemi, Robert R. Stephens, Henry O. Fuchs, “Metal Fatigue in Engineering”, 2nd edition, John Wiley & Sons Inc.; pp. 113-114, 2001.

14. F. Ellyin, “Fatigue Damage, Crack Growth and Life Prediction”, Springer Science & Business Media, pp. 135, 1997.

15. P. P. Milella, “Fatigue and Corrosion in Metals”, Springer, 2012.

16. T. G. Digges, S. J. Rosenberg, G. W. Geil, “Heat Treatment and Properties of Iron and Steel”, National Bureau of Standards Monograph 88, Issued November 1, Supersedes Circular 495 and Monograph 18, 1966.

17. W. E. Duckworth, G. Hoyle, “Electro-slag Refining”, Chapman and Hall, London, pp. 7–9, 1969.

18. S. K. Maity, N. B. Ballal, R. Kawalla, ISIJ. Int. 46, pp. 1361–1370, 2006.

19. Y. D. Li, Z. G. Yang, S. X. Li, Y. B. Liu, S. M. Chen: Acta Metall. Sin. 44, pp. 968–972, 2008.

20. S. J. Liu, Q. Y. Huang, C. J. Li, B. Huang: Fusion Eng. Des. 84, pp. 1214–1218, 2009.

21. J. D. Verhoeven, “Steel Metallurgy For The Non-Metallurgist”. ASM International, pp. 71-80, 2007.

22. G. E. Dieter, “Mechanical Metallurgy”, Mc Graw Hill Book Company, pp. 189-190, 1988.

23. O. O. Miller, “Influence of Austenitizing Time And Temperature On Austenite Grain Size Of Steel”, Trans. Am. Soc. Met., 43, pp. 261-287, 1951.

24. E. C. Bain, H. W. Paxton, “Alloying Elements In Steel”, 2nd edition, ASM, pp.37, 1961.

25. B. Pekgöz, S. Sarıdemir, İ. Uygur, Y. Aslan, “Sementasyon İşleminin Farklı Çeliklerin Mikroyapı ve Sertlik Değerlerine Etkileri”, Electronic Journal of Machine Technologies, Vol: 10, No: 1, pp.19-24, 2013.

26. TS EN ISO 6892-1 Standard, “Metallic Materials-Tensile testing-Part 1: Method Of Test At Room Temperature”.

27. Advanced Materials and Processes, ASM International,1990.

28. ASTM E23-12c, “Standard Test Methods for Notched Bar Impact Testing of Metallic Materials”, ASTM International, West Conshohocken, PA, 2012.

29. ASTM E10-12, “Standard Test Method for Brinell Hardness of Metallic Materials”, ASTM International, West Conshohocken, PA, 2012.

30. M. A. Razzak, “Effects Of Cr And Ni In Low Alloy Steel”, Bull. Mater. Sci., 34, No. 7, pp. 1439–1445, 2011.

31. R. W. Hertzberg, “Deformation And Fracture Mechanics Of Engineering Materials”, John Wiley & Sons Inc., 4th edition, 1996.

32. N. E. Dowling, “Fatigue Life and Inelastic Strain Response Under Complex Histories for an Alloy Steel” Journal of Testing and Evaluation, ASTM, Vol. 1, No. 4, pp. 271-287, July 1973.

33. C. Bathias, A. Pineau (editors) , “Fatigue Of Materials And Structures”, Wiley-ISTE, pp. 57, 2013.

34. R. Sanford, “Principles Of Fracture Mechanics”, NJ: Prentice Hall, Upper Saddle River, pp. 282-300, 2003.

35. R. O. Ritchie, B. Francis, W. L. Server, “Evaluation Of Toughness In AISI 4340 Alloy Steel Austenitized At Low And High Temperatures”, Metallurgical Transactions, Volume 7A, pp. 831, June 1976.

36. W. D. Callister, “Materials Science And Engineering: An Introduction”, 7th Edition, John Wiley & Sons Inc., 2007.

37. D. A. Virkler, B. M. Hillberry, P. K. Goel, “The Statistical Nature Of Fatigue Crack Propagation”, Technical Report AFFDL-TR-78-43, pp. 67, 1978.

38. MTS ®, http://www.mts.com/testsuite/multipurpose/fracture/crack_growth/ , last visited on March 2015.

39. H. E. Boyer, “Chapter 1, Practical Heat Treating”, 1st Edition, American Society for Metals, pp. 1–16, 1984.

40. G. Krauss, “Steels: Processing, Structure, And Performance”, ASM International, 2005.

41. “Practical Heat Treating, 2nd Edition, ASM International, Materials Park, Ohio, USA , Product Code: 05144G , 2006.

42. “Elements of Metallurgy and Engineering Alloys”, ASM International, Materials Park, Ohio, USA, Product Code: 05224G, “Chapter 14-Fatigue”, 2008.

43. A. Çalik, “Effect Of Cooling Rate On Hardness And Microstructure Of AISI 1020, AISI 1040 and AISI 1060 Steels”, International Journal of Physical Sciences Vol. 4 (9), pp. 514-518, September, 2009.

44. N. E. Dowling, C. A. Calhoun, A. Arcari, “Mean Stress Effects In Stress-Life Fatigue And The Walker Equation”, Blackwell Publishing Ltd., Fatigue & Fracture of Engineering Materials & Structures, 32, pp. 163–179, 2009.

45. N. E. Dowling, “Mean Stress Effects In Stress-Life And Strain-Life Fatigue”, Society of Automotive Engineers, Inc., F2004/51, 2004.

46. T. H. Courtney, “Mechanical Behavior Of Materials”, McGraw-Hill Book Co., pp. 566-629, 2000.

47. R. W. Honeycombe, “Steels – Microstructure And Properties”, Edward Arnold, 1981.

48. G. E. Totten, “Steel Heat Treatment Metallurgy And Technologies”, CRC Press, 2nd edition, 2007.

49. D. Hull, “Fractography: Observing, Measuring And Interpreting Fracture Surface Topography”, Cambridge University Press, 1999.

50. ASTM E399-90, “Standard Test Method for Plane-Strain Fracture Toughness of Metallic Materials”, American Society For Testing and Materials, 1997.

51. Total Materia, http://keytometals.com/page.aspx?ID=CheckArticle&site=kts&LN=TR&NM=393, last visited on: April 2015.

52. M. P. Nascimento, R. C. Souza, W. L. Pigatin, H. J. C. Voorwald, “Effects Of Surface Treatments On The Fatigue Strength Of AISI 4340 Aeronautical Steel”, International Journal of Fatigue 23, pp. 607–618, 2001.

53. K. B. Katnam, A. D. Crocombe, H. Khoramishad, I. A. Ashcroft, “Load Ratio Effect on the Fatigue Behaviour of Adhesively Bonded Joints: An Enhanced Damage Model”, Journal Of Adhesion, 86 (3), pp. 257 – 272, ISSN 0021-8464, 2010.

54. L. Alejandro, R. Arash, S. Karl-Gustaf, V. Esa, P. Braham; “Fatigue Of 0.55C-1.72Si Steel With Tempered Martensitic And Carbide-Free Bainitic Microstructures”, Acta Metallurgica Sinica (English Letters), 27(1), pp. 55-62, 2014.

APPENDIX A

SAMPLE PROGRAMME OUTPUT

Table A. A typical output of the programme based on C+, for Specimen Type: LR, R=0.1.

NO	CYCLES	A(MEAS.)	A(REG)	M.C.C.	DELTA K	da/dN
1	0	9.0				
2	375	9.1				
3	630	9.2				
4	1020	9.3	9.3026	0.9968	38.019435	3.279E-07
5	1335	9.4	9.4079	0.9968	38.299332	3.446E-07
6	1623	9.5	9.5058	0.9980	38.560315	3.727E-07
7	1818	9.6	9.5851	0.9979	38.772265	3.874E-07
8	2130	9.7	9.7124	0.9982	39.113567	4.009E-07
9	2325	9.8	9.7916	0.9982	39.326586	4.076E-07
10	2595	9.9	9.8991	0.9988	39.616580	4.074E-07
11	2844	10.0	10.0051	0.9992	39.903522	4.173E-07
12	3069	10.1	10.0959	0.9998	40.150124	4.169E-07
13	3312	10.2	10.1992	0.9998	40.431606	4.315E-07
14	3549	10.3	10.3020	0.9998	40.712736	4.433E-07
15	3774	10.4	10.4022	0.9999	40.987754	4.512E-07
16	3981	10.5	10.5005	0.9992	41.258539	4.484E-07
17	4194	10.6	10.5974	0.9995	41.526446	4.488E-07
18	4413	10.7	10.6949	0.9995	41.797017	4.420E-07
19	4677	10.8	10.8075	0.9994	42.110781	4.355E-07

20	4887	10.9	10.8959	0.9996	42.358103	4.401E-07
21	5127	11,0	11.0024	0.9995	42.657254	4.454E-07
22	5343	11.1	11.0995	0.9983	42.931163	4.741E-07
23	5547	11.2	11.1966	0.9985	43.206209	4.872E-07
24	5781	11.3	11.3146	0.9984	43.542025	5.074E-07
25	5919	11.4	11.3850	0.9984	43.743215	5.221E-07
26	6138	11.5	11.5044	0.9977	44.085909	5.243E-07
27	6324	11.6	11.6063	0.9985	44.379873	5.229E-07
28	6489	11.7	11.6878	0.9990	44.616003	5.054E-07
29	6716	11.8	11.8022	0.9985	44.949016	5.141E-07
30	6920	11.9	11.9047	0.9989	45.248974	5.131E-07
31	7115	12.0	12.0053	0.9985	45.544866	5.026E-07
32	7280	12.1	12.0919	0.9992	45.800792	5.095E-07
33	7484	12.2	12.1951	0.9990	46.107272	5.082E-07
34	7712	12.3	12.3058	0.9977	46.437879	5.220E-07
35	7901	12.4	12.4036	0.9983	46.731592	5.233E-07
36	8090	12.5	12.5037	0.9982	47.033838	5.532E-07
37	8231	12.6	12.5835	0.9977	47.275990	5.897E-07
38	8450	12.7	12.7182	0.9968	47.687213	6.036E-07
39	8585	12.8	12.8040	0.9962	47.950808	5.946E-07
40	8717	12.9	12.8813	0.9962	48.189419	5.858E-07
41	8915	13.0	13.0057	0.9984	48.575714	5.734E-07
42	9110	13.1	13.1047	0.9954	48.885204	5.381E-07
43	9275	13.2	13.1885	0.9966	49.148642	5.182E-07
44	9533	13.3	13.3208	0.9951	49.567343	5.454E-07
45	9650	13.4	13.3787	0.9935	49.751683	5.870E-07
46	9881	13.5	13.5178	0.9954	50.197345	7.022E-07
47	10001	13.6	13.6072	0.9940	50.485903	7.343E-07
48	10112	13.7	13.6917	0.9914	50.760212	7.247E-07
49	10226	13.8	13.7903	0.9989	51.082256	7.837E-07
50	10373	13.9	13.9016	0.9988	51.448372	7.359E-07

51	10529	14.0	14.0072	0.9982	51.798338	7.077E-07
52	10652	14.1	14.0909	0.9989	52.077561	6.964E-07
53	10823	14.2	14.2100	0.9987	52.477737	7.191E-07
54	10937	14.3	14.2900	0.9978	52.748461	7.601E-07
55	11090	14.4	14.4085	0.9977	53.152372	7.839E-07
56	11207	14.5	14.5059	0.9981	53.487012	8.133E-07
57	11303	14.6	14.5857	0.9977	53.763001	8.059E-07
58	11447	14.7	14.7060	0.9985	54.182217	8.265E-07
59	11560	14.8	14.7945	0.9982	54.493090	8.321E-07
60	11699	14.9	14.9098	0.9984	54.901318	8.233E-07
61	11804	15.0	14.9981	0.9981	55.216458	8.611E-07
62	11909	15.1	15.0873	0.9981	55.537064	8.902E-07
63	12050	15.2	15.2184	0.9981	56.012465	9.229E-07
64	12134	15.3	15.2945	0.9983	56.290760	9.355E-07
65	12236	15.4	15.3946	0.9969	56.659492	9.237E-07
66	12350	15.5	15.5059	0.9989	57.073111	9.365E-07
67	12446	15.6	15.5884	0.9987	57.382218	9.137E-07
68	12581	15.7	15.7095	0.9989	57.839912	9.210E-07
69	12683	15.8	15.8038	0.9989	58.199647	9.298E-07
70	12779	15.9	15.8952	0.9980	58.551158	9.116E-07
71	12887	16.0	15.9996	0.9997	58.956154	9.200E-07
72	12995	16.1	16.0925	0.9972	59.319725	9.169E-07
73	13124	16.2	16.2058	0.9979	59.767281	9.410E-07
74	13238	16.3	16.3109	0.9975	60.186605	1.050E-06
75	13313	16.4	16.3925	0.9959	60.514986	1.066E-06
76	13415	16.5	16.5117	0.9962	60.999195	1.097E-06
77	13475	16.6	16.5799	0.9954	61.278688	1.150E-06
78	13586	16.7	16.7048	0.9957	61.795273	1.136E-06
79	13685	16.8	16.8181	0.9957	62.269279	1.148E-06
80	13742	16.9	16.8811	0.9970	62.535114	1.126E-06
81	13844	17.0	17.0028	0.9980	63.053316	1.165E-06

82	13928	17.1	17.0977	0.9957	63.461760	1.211E-06
83	14018	17.2	17.2037	0.9981	63.922587	1.228E-06
84	14102	17.3	17.3097	0.9970	64.388379	1.356E-06
85	14156	17.4	17.3834	0.9971	64.715216	1.416E-06
86	14246	17.5	17.5191	0.9969	65.323535	1.496E-06
87	14291	17.6	17.5938	0.9961	65.662081	1.476E-06
88	14360	17.7	17.6915	0.9956	66.108889	1.453E-06
89	14429	17.8	17.7956	0.9965	66.590077	1.474E-06
90	14516	17.9	17.9178	0.9981	67.161802	1.382E-06
91	14570	18.0	17.9920	0.9981	67.512648	1.367E-06
92	14642	18.1	18.0879	0.9972	67.970315	1.384E-06
93	14729	18.2	18.2066	0.9946	68.543500	1.490E-06
94	14801	18.3				
95	14858	18.4				
96	14903	18.5				